

***Ab initio* tight-binding LMTO method for nonequilibrium electron transport in nanosystems**

Sergey V. Faleev,^{1,*} François Léonard,¹ Derek A. Stewart,^{1,†} and Mark van Schilfgaarde²

¹*Sandia National Laboratories, Livermore, California 94551, USA*

²*Department of Chemical and Materials Engineering, Arizona State University, Tempe, Arizona 85284, USA*

(Received 4 January 2005; revised manuscript received 25 February 2005; published 31 May 2005)

We present an *ab initio* method for calculation of the electronic structure and electronic transport of nanoscale systems coupled to electrodes with applied voltage bias. The method is based on the local density approximation of density functional theory and implemented in the framework of the tight-binding linear muffin-tin orbital approach in its atomic sphere approximation. A fully atomistic description of the electrodes and the nanosystem is used, and the self-consistent charge and electrostatic potential for the system under applied bias is calculated using the nonequilibrium Green's function (NEGF) approach. General expressions for the lesser Green's function and transmission coefficient obtained within NEGF theory are rewritten using auxiliary Green's functions that are defined by the inverse of the short-ranged structural constants. This reformulation of the theory with auxiliary Green's functions allows the use of very effective and well-developed tight-binding techniques. The method is applied to three systems: a single benzene di-thiol molecule coupled to (111) gold electrodes, a single gold atom coupled to (100) gold electrodes, and a single platinum atom coupled to (100) platinum electrodes.

DOI: 10.1103/PhysRevB.71.195422

PACS number(s): 72.10.-d, 73.63.-b, 73.63.Rt, 85.65.+h

I. INTRODUCTION

Recent experimental developments have made it possible to fabricate electronic devices where the active part is a molecule, a nanotube, or a similar structure of nanometer-scale dimension. These developments have given rise to growing interest in theoretical methods that can calculate the electronic structure and transport properties of nanoscale devices. By nature, first-principles quantum-mechanical approaches are necessary for such calculations because quantum effects dominate the transport properties of these nanoscale systems. The first-principles electronic structure methods available today are highly developed and sophisticated but are implemented mostly to describe systems that are (1) in equilibrium and (2) either periodic or have a finite number of atoms. However, nanoscale systems connected to bulk electrodes should be described by methods that can treat nonperiodic and infinite size *open* systems. Additionally, in the presence of finite voltage bias applied across the electrodes, the system is out of equilibrium. The required theoretical methods should properly describe this nonequilibrium situation.

The first *ab initio* nonequilibrium calculations for an open system were performed by using a jellium approximation for the electrodes.^{1,2} Other approaches have used a first-principles Hamiltonian for the nanostructure and semiempirical approximations to describe the electrodes for an equilibrium system³⁻⁶ or a system with applied bias voltage.⁷⁻⁹ Still other approaches employed first-principles treatment of both a nanosystem and electrodes for a system in equilibrium^{10,11} or a system at finite applied bias described by nonself-consistent electrostatic potential.¹²⁻¹⁵ Three methods that allow first-principles treatment of both a nanosystem and electrodes in the nonequilibrium situation have been proposed recently by Damle *et al.*¹⁶ (implemented on the basis of GAUSSIAN98 quantum chemistry software), by Taylor *et*

al.^{17,18} (implemented in the simulation package MDCAL) and by Brandbyge *et al.*¹⁹ (implemented in the simulation package TRANSIESTA). All three of these methods use a pseudopotential approximation for the core electrons and the local density approximation (LDA) for the exchange-correlation potential. These three approaches have been applied to calculations of electronic structure and transport properties of different nanosystems.¹⁶⁻²⁹

An entirely different first-principles approach based on the tight-binding linear muffin-tin orbital method (TB-LMTO)³⁰ has been proposed by Kudrnovsky *et al.*³¹ and Turek *et al.*³² for description of *equilibrium* transport properties of a nanoscale system connected to two electrodes. Starting with the Kubo-Greenwood formulation of equilibrium transport theory, they derived an expression for the conductance in the framework of the TB-LMTO method in its atomic sphere approximation (ASA). The LMTO method is an all-electron method which does not use the pseudopotential approximation. The advantage of an all-electron method over the pseudopotential method, beyond the fact that the latter one is an approximation to the former, is that the problem of constructing the potentials for *magnetic* systems can be solved straightforwardly in an all-electron calculation, while for pseudopotential methods this problem constitutes a real challenge if traditional norm-conserving or ultrasoft pseudopotentials are used.³³ The equilibrium TB-LMTO-ASA transport theory of Kudrnovsky *et al.* has been applied recently, mainly to magnetic systems, to study magnetotransport in metallic multilayers,^{31,34} resistivity of bulk random alloys,³² resonant tunneling magnetoresistance,³⁵ and spin-dependent tunneling in metal/vacuum/metal systems.³⁶

The aim of this paper is to formulate a theory based on the TB-LMTO-ASA method that can be used for self-consistent calculations of the electronic structure and transport properties of an open system in the *nonequilibrium* situation. This

theory can be applied to calculate current-voltage curves for a nanoscale system connected to two electrodes. Beyond this, such a theory may be considered as a first step to formulate a more accurate full-potential version (without atomic spheres approximation) of a TB-LMTO method for an open system out of equilibrium.

The starting point of our implementation is a principal layers TB-LMTO-ASA code³⁷ that exploits equilibrium Green's functions techniques. This code has been tested for several systems^{35–37} and results are in good agreement with full-potential equilibrium LMTO calculations.³⁸ The advantage of the tight-binding formulation of the LMTO-ASA method³⁰ is that effectively only a few nearest neighbor atoms interact with each other, thus making numerical computations very efficient.

The organization of the paper is as follows. In Sec. II we derive the expressions for electron density and current based on the nonequilibrium Green's function formulation of TB-LMTO-ASA method. Section III describes numerical procedures of the implementation. In Sec. IV we apply our method to calculate the electronic structure and current-voltage curve for three systems: a single benzene di-thiol molecule coupled to semi-infinite gold electrodes, a single gold atom coupled to semi-infinite gold electrodes, and a single platinum atom coupled to semi-infinite platinum electrodes. We compare results presented in Sec. IV with other *ab initio* calculations and existing experimental results. Conclusions are presented in Sec. V.

II. THEORY OF NONEQUILIBRIUM ELECTRON TRANSPORT IN THE TB-LMTO-ASA FRAMEWORK

A. System description and introduction to the TB-LMTO-ASA method

The system is defined by an infinite set of atomic positions $\{\mathbf{R}\}$. We partition the system in principal layers as follows: the semi-infinite left lead has principal layer indices $p=0, -1, -2, \dots, -\infty$, the central region of the system has indices $p=1, \dots, N$, and the semi-infinite right lead has indices $p=N+1, N+2, \dots, +\infty$. The width of each layer is chosen in such a way that only adjacent layers interact with each other. The total size of the central region (or the number N of principal layers) is chosen so that all charge and potential relaxations take place in the central region and lead regions have charge and potential close to the bulk values. The results of numerical simulations can be verified by including more layers from the lead regions in the central region and by increasing the width of individual layers. The left and right leads may in general be of different atomic compositions, and are assumed to be in thermal equilibrium with chemical potentials μ_L and μ_R , respectively. The difference between chemical potentials $\mu_R - \mu_L = eV$ defines the voltage bias V applied to the leads, where e is the electron charge.

The basic blocks of the linear muffin-tin orbitals^{30,39} (LMTO's) are functions defined inside each atomic (Wigner-Seitz) sphere centered at site \mathbf{R} , namely,

$$\phi_{\mathbf{R}L}(\mathbf{r}) = \phi_{\mathbf{R}l}(r)Y_L(\hat{\mathbf{r}}), \quad (1)$$

$$\dot{\phi}_{\mathbf{R}L}(\mathbf{r}) = \dot{\phi}_{\mathbf{R}l}(r)Y_L(\hat{\mathbf{r}}),$$

where the radial amplitude $\phi_{\mathbf{R}l}(r)$ is a regular solution of the radial Schrödinger equation (or scalar Dirac equation) inside the sphere at a linearization energy $E_{v,\mathbf{R}l}$, and $\dot{\phi}_{\mathbf{R}l}(r)$ is the first energy derivative of $\phi_{\mathbf{R}l}(r)$. In the ASA, the potential entering the Schrödinger equation is assumed to be spherically symmetric in each sphere. The potential is a sum of contributions from nuclei, Hartree, and LDA exchange-correlation potentials. The functions $Y_L(\hat{\mathbf{r}})$ in Eq. (1) are real spherical harmonics, $\hat{\mathbf{r}} = \mathbf{r}/r$, and $L = \{l, m\}$ is an orbital momentum index. We will ignore the spin index throughout this paper for the sake of brevity, although it can be trivially reconstructed: All matrix quantities (i.e. Hamiltonian, Green's functions) are diagonal in the spin index. The radial amplitudes satisfy standard normalization and orthogonality relations^{30,39}

$$\int_0^{s_{\mathbf{R}}} \phi_{\mathbf{R}l}^2(r)r^2 dr = 1, \quad \int_0^{s_{\mathbf{R}}} \phi_{\mathbf{R}l}(r)\dot{\phi}_{\mathbf{R}l}(r)r^2 dr = 0, \quad (2)$$

where $s_{\mathbf{R}}$ denotes the radius of the \mathbf{R} th sphere. In the ASA, the interstitial part of the orbital is omitted and the functions $\phi_{\mathbf{R}l}(r)$ and $\dot{\phi}_{\mathbf{R}l}(r)$ are set to zero outside the \mathbf{R} th sphere. Using the notation $\mathbf{r}_{\mathbf{R}} = \mathbf{r} - \mathbf{R}$ an orthonormal basis of LMTO's $\{\chi_{\mathbf{R}L}(\mathbf{r})\}$ reads

$$\chi_{\mathbf{R}L}(\mathbf{r}) = \phi_{\mathbf{R}L}(\mathbf{r}_{\mathbf{R}}) + \sum_{\mathbf{R}'L'} \dot{\phi}_{\mathbf{R}'L'}(\mathbf{r}_{\mathbf{R}'})h_{\mathbf{R}'L',\mathbf{R}L}, \quad (3)$$

where $h_{\mathbf{R}'L',\mathbf{R}L}$ is a real symmetric matrix defined in a standard way.^{30,40} The first term on the right-hand side of Eq. (3) represents the head of the LMTO's and the second term represents the tail.

The second-order TB-LMTO-ASA Hamiltonian in the orthonormal basis given by Eq. (3) reads^{30,40}

$$H_{\mathbf{R}L,\mathbf{R}'L'} = C_{\mathbf{R}L}\delta_{\mathbf{R}L,\mathbf{R}'L'} + \sqrt{\Delta_{\mathbf{R}L}} \times \{S^\alpha [1 + (\alpha - \gamma)S^\alpha]^{-1}\}_{\mathbf{R}L,\mathbf{R}'L'} \sqrt{\Delta_{\mathbf{R}'L'}}, \quad (4)$$

where the real constants $C_{\mathbf{R}L}$, $\Delta_{\mathbf{R}L}$, and $\gamma_{\mathbf{R}L}$ are standard potential parameters. The superscript α denotes a LMTO representation defined by a set of screening constants $\alpha_{\mathbf{R}L}$, and $S_{\mathbf{R}L,\mathbf{R}'L'}^\alpha$ is a real symmetric matrix of screened structural constants in the α representation. The Hamiltonian in Eq. (4) is invariant with respect to the LMTO representation, so with suitable choice of $\alpha_{\mathbf{R}L}$ the screened structural constant matrix can typically be reduced to the second-nearest neighbors for close-packed lattices.³⁰ It can be shown^{30,40} that the Hamiltonian in Eq. (4) is related to the coefficients $h_{\mathbf{R}'L',\mathbf{R}L}$ of Eq. (3) by a simple diagonal shift

$$H_{\mathbf{R}L,\mathbf{R}'L'} = E_{v,\mathbf{R}l}\delta_{\mathbf{R}L,\mathbf{R}'L'} + h_{\mathbf{R}L,\mathbf{R}'L'}. \quad (5)$$

B. Charge density of a nonequilibrium system in LMTO-ASA approach

Within the NEGF approach the electron density distribution can be obtained by

$$\rho(\mathbf{r}) = -i \frac{1}{2\pi} \sum_{\mathbf{R}\mathbf{L}} \sum_{\mathbf{R}'\mathbf{L}'} \int dE \chi_{\mathbf{R}\mathbf{L}}(\mathbf{r}) G_{\mathbf{R}\mathbf{L},\mathbf{R}'\mathbf{L}'}^<(E) \chi_{\mathbf{R}'\mathbf{L}'}(\mathbf{r}). \quad (6)$$

The lesser Green's function is defined as⁴¹

$$G_{\mathbf{R}\mathbf{L},\mathbf{R}'\mathbf{L}'}^<(E) = \frac{i}{\hbar} \int d(t-t') e^{iE(t-t')/\hbar} \langle c_{\mathbf{R}'\mathbf{L}'}^\dagger(t') c_{\mathbf{R}\mathbf{L}}(t) \rangle, \quad (7)$$

where $c_{\mathbf{R}\mathbf{L}}^\dagger(t')$ and $c_{\mathbf{R}\mathbf{L}}(t)$ are Heisenberg's operators for creation and annihilation of an electron in the $\chi_{\mathbf{R}\mathbf{L}}$ state.

For sites \mathbf{R} and \mathbf{R}' within the central region, the lesser Green's function is given by⁴²

$$\begin{aligned} G_{\mathbf{c}\mathbf{B}\mathbf{L},\mathbf{c}'\mathbf{B}'\mathbf{L}'}^<(E) &= i \sum_{c_1=1}^N \sum_{c_2=1}^N \left\{ G_{\mathbf{c}\mathbf{B}\mathbf{L},c_1\mathbf{B}_1\mathbf{L}_1}(E_+) \right. \\ &\quad \times [f_{\mathcal{L}}(E) \Gamma_{c_1\mathbf{B}_1\mathbf{L}_1,c_2\mathbf{B}_2\mathbf{L}_2}^{\mathcal{L}}(E) \\ &\quad + f_{\mathcal{R}}(E) \Gamma_{c_1\mathbf{B}_1\mathbf{L}_1,c_2\mathbf{B}_2\mathbf{L}_2}^{\mathcal{R}}(E)] \\ &\quad \left. \times G_{c_2\mathbf{B}_2\mathbf{L}_2,c'\mathbf{B}'\mathbf{L}'}(E_-) \right\}. \end{aligned} \quad (8)$$

The Fermi-Dirac distributions for the left and right leads $f_{\mathcal{L}}(E)$ and $f_{\mathcal{R}}(E)$ are defined with chemical potentials $\mu_{\mathcal{L}}$ and $\mu_{\mathcal{R}}$, respectively. In Eq. (8) we decompose the index of the site \mathbf{R} in the combination $\mathbf{R} = \{p, \mathbf{B}\}$, where p is a principal layer index and \mathbf{B} is the index of an atom in principal layer p . Here and below we assume the following convention for the indices of principal layers: indices denoted as c, c', c'' are indices corresponding to the central region and run from 1 to N , indices denoted as l, l', l'' are indices corresponding to the left lead and run from $-\infty$ to 0, indices denoted as r, r', r'' are indices corresponding to the right lead and run from $N+1$ to $+\infty$, and indices denoted as p, p', p'' are indices corresponding to the entire system and run from $-\infty$ to $+\infty$. Summation is implied over repeating indices $\mathbf{B}_1\mathbf{L}_1$ and $\mathbf{B}_2\mathbf{L}_2$ in Eq. (8). In what follows we will omit indices $\mathbf{B}\mathbf{L}$ and assume that all corresponding quantities are matrices in these indices (matrix representation). Energies E_+ and E_- have infinitesimally small complex parts $E_{\pm} = E \pm i0$, so $G(E_+)$ and $G(E_-)$ are well-known retarded and advanced Green's functions. The Green's function $G_{p,p'}(z)$ of complex energy z is defined as the inverse of the Hamiltonian of Eq. (4) of the entire system

$$\sum_{p'=-\infty}^{+\infty} (z \delta_{p,p'} - H_{p,p'}) G_{p',p''}(z) = \delta_{p,p''}. \quad (9)$$

Matrices $\Gamma_{c,c'}^{\mathcal{L}/\mathcal{R}}(E)$ in Eq. (8) read

$$\Gamma_{c,c'}^{\mathcal{L}/\mathcal{R}}(E) = i \left[\Sigma_{c,c'}^{\mathcal{L}/\mathcal{R}}(E_+) - \Sigma_{c,c'}^{\mathcal{L}/\mathcal{R}}(E_-) \right], \quad (10)$$

where the so-called self-energy terms $\Sigma_{c,c'}^{\mathcal{L}}$ and $\Sigma_{c,c'}^{\mathcal{R}}$ represent the interaction with the left and right leads, and are defined as

$$\Sigma_{c,c'}^{\mathcal{L}}(z) = \sum_{l < 1} \sum_{l' < 1} H_{c,l} G_{l,l'}^{\mathcal{L}}(z) H_{l',c'}, \quad (11)$$

$$\Sigma_{c,c'}^{\mathcal{R}}(z) = \sum_{r > N} \sum_{r' > N} H_{c,r} G_{r,r'}^{\mathcal{R}}(z) H_{r',c'}. \quad (12)$$

Here the Green's function of the left (right) lead is defined as the inverse of the Hamiltonian in Eq. (4) with all matrix elements with indices outside the left (right) lead set to zero

$$\sum_{l' < 1} (z \delta_{l,l'} - H_{l,l'}) G_{l',l''}^{\mathcal{L}}(z) = \delta_{l,l''} \quad (13)$$

$$\sum_{r' > N} (z \delta_{r,r'} - H_{r,r'}) G_{r',r''}^{\mathcal{R}}(z) = \delta_{r,r''}. \quad (14)$$

Note that $G(z)$, $G^{\mathcal{L}}(z)$, $G^{\mathcal{R}}(z)$, and hence $G^<(z)$ are invariant with respect to the LMTO representation because the Hamiltonian is invariant.

If both indices \mathbf{R} and \mathbf{R}' of the lesser Green's function in Eq. (6) belong to the left (right) lead, then the equilibrium formula for the lesser Green's function can be applied⁴¹

$$G_{\mathbf{R}\mathbf{L},\mathbf{R}'\mathbf{L}'}^<(E) = f(E) [G_{\mathbf{R}\mathbf{L},\mathbf{R}'\mathbf{L}'}(E_-) - G_{\mathbf{R}\mathbf{L},\mathbf{R}'\mathbf{L}'}(E_+)], \quad (15)$$

where $f(E) = f_{\mathcal{L}}(E)$ for the left lead and $f(E) = f_{\mathcal{R}}(E)$ for the right lead.

In Appendix A we show that Eq. (6) can be rewritten in terms of diagonal elements of the lesser Green's function

$$\begin{aligned} \rho(\mathbf{r}) &= -i \frac{1}{2\pi} \sum_{\mathbf{L}\mathbf{L}'} \int dE [\phi_{\mathbf{R}\mathbf{L}}(\mathbf{r}_{\mathbf{R}}) + \dot{\phi}_{\mathbf{R}\mathbf{L}}(\mathbf{r}_{\mathbf{R}})(E - E_{\nu,\mathbf{R}})] \\ &\quad \times G_{\mathbf{R}\mathbf{L},\mathbf{R}\mathbf{L}'}^<(E) [\phi_{\mathbf{R}\mathbf{L}'}(\mathbf{r}_{\mathbf{R}}) + \dot{\phi}_{\mathbf{R}\mathbf{L}'}(\mathbf{r}_{\mathbf{R}})(E - E_{\nu,\mathbf{R}'})], \end{aligned} \quad (16)$$

where the index \mathbf{R} labels a sphere which contains the vector \mathbf{r} . In the ASA, the charge-density distribution inside each sphere is assumed to be spherically symmetric, thus the angle averaged expression for the radial charge distribution inside the \mathbf{R} th sphere takes the form

$$\begin{aligned} \rho_{\mathbf{R}}(r) &\equiv \frac{1}{4\pi} \int d\hat{\mathbf{r}} \rho_{\mathbf{R}}(\mathbf{r}) \\ &= -i \frac{1}{8\pi^2} \sum_{\mathbf{L}} \int dE G_{\mathbf{R}\mathbf{L},\mathbf{R}\mathbf{L}}^<(E) \\ &\quad \times [\phi_{\mathbf{R}\mathbf{L}}(r) + \dot{\phi}_{\mathbf{R}\mathbf{L}}(r)(E - E_{\nu,\mathbf{R}})]^2. \end{aligned} \quad (17)$$

In equilibrium, when $f_{\mathcal{L}}(E) = f_{\mathcal{R}}(E) = f(E)$, the lesser Green's function takes the standard form (15) and the expression for the charge density (17) reduces to

$$\rho_{\mathbf{R}}(r) = -\frac{1}{4\pi^2} \sum_L \int dE f(E) \text{Im}\{G_{\mathbf{R}L,\mathbf{R}L}(E_+)\} \times [\phi_{\mathbf{R}l}(r) + \dot{\phi}_{\mathbf{R}l}(r)(E - E_{\nu,\mathbf{R}l})]^2. \quad (18)$$

One can see that expression (18) is a linearized approximation to the exact charge-density formula for a system in equilibrium

$$\rho_{\mathbf{R}}^{\text{KKR}}(r) \equiv -\frac{1}{4\pi^2} \sum_L \int dE f(E) \text{Im}\{G_{\mathbf{R}L,\mathbf{R}L}(E_+)\} \phi_{\mathbf{R}l}^2(E; r), \quad (19)$$

obtained by the multiple scattering method of Korringa, Kohn and Rostoker (KKR).⁴⁰ Here $\phi_{\mathbf{R}l}(E; r)$ is the solution of the radial Schrödinger equation inside sphere \mathbf{R} at energy E . To minimize the error introduced by the linearization, $E_{\nu,\mathbf{R}l}$ in our approach is chosen in the center of gravity of $G_{\mathbf{R}L,\mathbf{R}L}^<(E)$ for each sphere \mathbf{R} and angular momentum l

$$\sum_{m=-l}^l \int dE G_{\mathbf{R}L,\mathbf{R}L}^<(E)(E - E_{\nu,\mathbf{R}l}) = 0. \quad (20)$$

C. Tight-binding formulation of LMTO-ASA

Expressions (8)–(14) and (17) completely define the charge density of the system under nonequilibrium conditions, but they are not suitable for practical applications. Structural constants in the maximally screened representations are shortranged, but the Hamiltonian in Eq. (4) is significantly longer ranged, so it is computationally very demanding to construct the Hamiltonian from known structural constants, to solve directly for the Green's functions, and to determine $\Gamma_{c,c'}^{\mathcal{L}/\mathcal{R}}(E)$ for all principal layers in the central region. In order to take advantage of the short-ranged structural constants, one needs to rewrite the expression for the lesser Green's function (8) in terms of so-called auxiliary Green's functions⁴⁰ which can be found by tight-binding techniques the same way as it is done in equilibrium.

In order to address this problem let us introduce step matrices Q^0 and Q^N , which are diagonal in all indices $p\mathbf{B}L$ with diagonal elements given by $Q_{p,p}^0 = 1$ for $p > 0$, and $Q_{p,p}^0 = 0$ for $p \leq 0$, and, analogously, $Q_{p,p}^N = 1$ for $p > N$, and $Q_{p,p}^N = 0$ for $p \leq N$. The matrix Q^i ($i=0$ or N) can be interpreted as an operator of the number of electrons that populate principal layers with $p > i$. It is easy to see that

$$\begin{aligned} & \sum_{p=-\infty}^{\infty} \sum_{p'=-\infty}^{\infty} G_{c,p}(E_+) [Q^0, H]_{p,p'} G_{p',c'}(E_-) \\ &= \sum_{l < 1} \sum_{c''=1}^N [G_{c,c''}(E_+) H_{c'',l} G_{l,c'}(E_-) \\ & \quad - G_{c,l}(E_+) H_{l,c''} G_{c'',c'}(E_-)], \end{aligned} \quad (21)$$

where $[Q, H] = QH - HQ$ denotes the commutator of two matrices. We assume here that the matrix elements of the Hamiltonian between the left and right leads vanish. The

Green's functions with mixed indices $G_{l,c}$ and $G_{c,l}$ can be expressed in terms of surface Green's function and Green's function of the central region by using the Dyson equations

$$G_{l,c}(z) = \sum_{l' < 1} \sum_{c'=1}^N G_{l,l'}^{\mathcal{L}}(z) H_{l',c'} G_{c',c}(z), \quad (22)$$

$$G_{c,l}(z) = \sum_{l' < 1} \sum_{c'=1}^N G_{c,c'}(z) H_{c',l'} G_{l',l}^{\mathcal{L}}(z).$$

Applying Eq. (22) to Eq. (21) and using the definition of $\Gamma_{c_1,c_2}^{\mathcal{L}}$ one can find

$$\begin{aligned} & \sum_{p=-\infty}^{\infty} \sum_{p'=-\infty}^{\infty} G_{c,p}(E_+) [Q^0, H]_{p,p'} G_{p',c'}(E_-) \\ &= i \sum_{c_1=1}^N \sum_{c_2=1}^N G_{c,c_1}(E_+) \Gamma_{c_1,c_2}^{\mathcal{L}}(E) G_{c_2,c'}(E_-). \end{aligned} \quad (23)$$

Using the matrix Q^N instead of Q^0 yields an analogous equality for the right lead. Thus, the expression (8) for the lesser Green's function can be rewritten in the form

$$\begin{aligned} G_{c,c'}^<(E) &= \sum_{p=-\infty}^{\infty} \sum_{p'=-\infty}^{\infty} G_{c,p}(E_+) \{f_{\mathcal{L}}(E) [Q^0, H] \\ & \quad - f_{\mathcal{R}}(E) [Q^N, H]\}_{p,p'} G_{p',c'}(E_-). \end{aligned} \quad (24)$$

In the full matrix notation, where we omit all indices including the principal layer index, the Hamiltonian reads

$$H = C + \sqrt{\Delta} S^\alpha [1 + (\alpha - \gamma) S^\alpha]^{-1} \sqrt{\Delta}. \quad (25)$$

The commutator of Q^i with the Hamiltonian takes the form

$$[Q^i, H] = \sqrt{\Delta} [1 + S^\alpha (\alpha - \gamma)]^{-1} [Q^i, S^\alpha] [1 + (\alpha - \gamma) S^\alpha]^{-1} \sqrt{\Delta}, \quad (26)$$

where we used the fact that C , Δ , γ , α , and Q^i are diagonal matrices with respect to $p\mathbf{B}L$ indices. Using the definition of the Green's function $G(z) = [z - H]^{-1}$ one can obtain

$$\begin{aligned} & [1 + (\alpha - \gamma) S^\alpha]^{-1} \sqrt{\Delta} G(z) \\ &= [(z - C) / \sqrt{\Delta} (1 + (\alpha - \gamma) S^\alpha) - \sqrt{\Delta} S^\alpha]^{-1} \\ &= g^\alpha(z) [\Delta + (\gamma - \alpha)(z - C)]^{-1} \sqrt{\Delta}. \end{aligned} \quad (27)$$

Here $g^\alpha(z)$ is the so-called auxiliary Green's function defined as the inverse of the short-ranged matrix $P^\alpha(z) - S^\alpha$

$$\sum_{p'=-\infty}^{+\infty} (P_p^\alpha(z) \delta_{p,p'} - S_{p,p'}^\alpha) g_{p',p''}^\alpha(z) = \delta_{p,p''}. \quad (28)$$

The potential function $P^\alpha(z)$ is diagonal over $p\mathbf{B}L$ indices, and is defined as

$$P^\alpha(z) = (z - C) [\Delta + (\gamma - \alpha)(z - C)]^{-1}. \quad (29)$$

Similarly to equality (27) one may obtain

$$G(z)\sqrt{\Delta}[1+S^\alpha(\alpha-\gamma)]^{-1}=\sqrt{\Delta}[\Delta+(\gamma-\alpha)(z-C)]^{-1}g^\alpha(z). \quad (30)$$

Utilizing equalities (27) and (30) the lesser Green's function (24) can be rewritten as

$$G_{c,c'}^<(E)=\{\mu^\alpha(E_+)g^\alpha(E_+)(f_{\mathcal{L}}(E)[Q^0,S^\alpha]-f_{\mathcal{R}}(E)[Q^N,S^\alpha])g^\alpha(E_-)\mu^\alpha(E_-)\}_{c,c'}, \quad (31)$$

where the diagonal matrix $\mu^\alpha(z)$ is defined by

$$\mu^\alpha(z)=\sqrt{\Delta}[\Delta+(\gamma-\alpha)(z-C)]^{-1}. \quad (32)$$

It can be shown that expression (31) does not have a singularity at $\Delta+(\gamma-\alpha)(z-C)=0$. Algebraically, Eq. (31) looks exactly the same as Eq. (24) with $P^\alpha(z)-S^\alpha$ taking the place of $z-H$. Similarly, the equivalent of Eq. (8) is

$$G_{c,c'}^<(E)=\mu_c^\alpha(E)\{f_{\mathcal{L}}(E)g_{c,1}^\alpha(E_+)\Gamma_{1,1}^\alpha(E)g_{1,c'}^\alpha(E_-)+f_{\mathcal{R}}(E)g_{c,N}^\alpha(E_+)\Gamma_{N,N}^\alpha(E)g_{N,c'}^\alpha(E_-)\}\mu_{c'}^\alpha(E). \quad (33)$$

In the maximally screened LMTO representation the structural constants S^α connect only adjacent layers, $S_{p,p'}^\alpha=0$ for $|p-p'|>1$; hence the Γ^α matrix that appears in Eq. (33) has only two nonzero components $\Gamma_{1,1}^\alpha$ and $\Gamma_{N,N}^\alpha$ defined as

$$\Gamma_{1,1}^\alpha(E)=iS_{1,0}^\alpha[g_{0,0}^{\alpha\mathcal{L}}(E_+)-g_{0,0}^{\alpha\mathcal{L}}(E_-)]S_{0,1}^\alpha, \quad (34)$$

$$\Gamma_{N,N}^\alpha(E)=iS_{N,N+1}^\alpha[g_{N+1,N+1}^{\alpha\mathcal{R}}(E_+)-g_{N+1,N+1}^{\alpha\mathcal{R}}(E_-)]S_{N+1,N}^\alpha.$$

Here the surface auxiliary Green's function of the left (right) lead is defined as the inverse of the $P^\alpha(z)-S^\alpha$ matrix which has all matrix elements with indices outside the left (right) lead set to zero

$$\sum_{l'<1}[P_l^\alpha(z)\delta_{l,l'}-S_{l,l'}^\alpha]g_{l',m}^{\alpha\mathcal{L}}(z)=\delta_{l,m}, \quad (35)$$

$$\sum_{r'>N}[P_r^\alpha(z)\delta_{r,r'}-S_{r,r'}^\alpha]g_{r',m}^{\alpha\mathcal{R}}(z)=\delta_{r,m}. \quad (36)$$

Equations (33) and (34) that define the lesser Green's function in terms of auxiliary Green's function and surface auxiliary Green's functions form the central part of this work. The matrix $P^\alpha(z)-S^\alpha$ is tridiagonal in the principal layer indices. This allows the use of well developed^{30,37,40,42-45} and very efficient tight-binding LMTO approaches to calculate the auxiliary Green's function $g_{c,c'}^\alpha(z)$ in the center region and surface auxiliary Green's functions $g_{0,0}^{\alpha\mathcal{L}}(z)$ and $g_{N+1,N+1}^{\alpha\mathcal{R}}(z)$. The charge density can be calculated then by using Eq. (17).

One may verify that in equilibrium [$f_{\mathcal{L}}(E)=f_{\mathcal{R}}(E)=f(E)$] Eq. (33) takes the standard form⁴¹

$$G^<(E)=-2if(E)\text{Im}[G(E_+)]. \quad (37)$$

Importantly, formula (37) remains true even in the nonequilibrium situation for energies E such that the equality $f_{\mathcal{L}}(E)=f_{\mathcal{R}}(E)$ is satisfied.

D. Transmission coefficient and current in TB-LMTO-ASA

The current density can be obtained as

$$I=\frac{e}{A}\frac{d}{dt}\langle\hat{Q}^0(t)\rangle, \quad (38)$$

where A is the cross-sectional area of the system in a plane perpendicular to the direction of the current and \hat{Q}^0 is an operator of the total number of electrons in principal layers $p>0$

$$\hat{Q}^0(t)=\sum_{p=-\infty}^{\infty}\sum_{\mathbf{BL}}Q_{p\mathbf{BL},p\mathbf{BL}}^0c_{p\mathbf{BL}}^\dagger(t)c_{p\mathbf{BL}}(t). \quad (39)$$

Eq. (38) can be rewritten as

$$I=-i\frac{e}{\hbar A}\langle[\hat{Q}^0,\hat{H}]\rangle =\frac{2e}{h}\int dE\sum_{p>0}\sum_{l<1}\text{tr}\{H_{l,p}G_{p,l}^<(E)-H_{p,l}G_{l,p}^<(E)\}, \quad (40)$$

where $\text{tr}\{\dots\}$ means trace over indices \mathbf{BL} , and the factor of 2 is for spin degeneracy. If the Hamiltonian is not spin degenerate the trace in Eq. (40) is also taken over spins. It can be shown⁴² that expression (40) can be transformed to the Meir-Wingreen form⁴⁶

$$I=\frac{2e}{hA}\int dET(E,V)[f_{\mathcal{L}}(E)-f_{\mathcal{R}}(E)], \quad (41)$$

where $T(E,V)$ is the transmission coefficient for the system with finite bias voltage V applied to the electrodes, and given by⁴²

$$T(E,V)=\sum_{c_1=1}^N\sum_{c_2=1}^N\sum_{c_3=1}^N\sum_{c_4=1}^N\text{tr}\{\Gamma_{c_1,c_2}^{\mathcal{L}}(E)G_{c_2,c_3}(E_+) \times \Gamma_{c_3,c_4}^{\mathcal{R}}(E)G_{c_4,c_1}(E_-)\}. \quad (42)$$

We show explicitly the dependence of the transmission coefficient $T(E,V)$ on applied voltage V in order to stress that it should be calculated for the nonequilibrium system whose charge density and electrostatic potentials are found self-consistently by using the theory described above.

In Appendix B we derive an expression for the transmission (42) in terms of the auxiliary Green's functions obtained in the maximally screened LMTO representation

$$T(E,V)=\text{tr}\{\Gamma_{1,1}^\alpha(E)g_{1,N}^\alpha(E_+)\Gamma_{N,N}^\alpha(E)g_{N,1}^\alpha(E_-)\}. \quad (43)$$

Note that the transmission (43) is invariant with respect to the LMTO representation by construction [see definition (42)]. In the linear response regime, when the applied voltage is small, the conductance takes the form

$$C=\frac{I}{V}=\frac{2e^2}{hA}T(E_F,V=0), \quad (44)$$

where E_F is the Fermi energy of the entire system in equilibrium. Expressions (43) and (44) for conductance coincide with that obtained by Kudrnovsky *et al.*³¹ and Turek *et al.*³²

within the Kubo-Greenwood framework for equilibrium systems. Note, that our derivation of the expression for the transmission coefficient (43) obtained within the NEGF formalism does not exploit the approximation of piecewise constant coordinate that was used in Ref. 32.

The equations for the lesser Green's function (33) and the transmission coefficient (43) can be directly used for calculations of the ASA charge-density distribution (17) and current density (41) for systems with a finite number of atoms in each principal layer. In the case when the system has two-dimensional translational invariance in the xy plane (plane perpendicular to the principal layers growth direction, the z axis) these formulas may be easily modified. Let us assume one and the same two-dimensional translational symmetry in each principal layer. Then the Hamiltonian can be transformed to the \mathbf{k} representation

$$H_{p\mathbf{B}L,p'\mathbf{B}'L'}(\mathbf{k}) = \sum_{\mathbf{T}_{\parallel}} H_{p\mathbf{B}L,p'(\mathbf{B}'+\mathbf{T}_{\parallel})L'} e^{i\mathbf{k}\mathbf{T}_{\parallel}}. \quad (45)$$

Here \mathbf{k} is a two-dimensional vector in the xy plane from the corresponding surface Brillouin zone (SBZ), and the index of site \mathbf{R} is rewritten in the form $\mathbf{R}=(p,\mathbf{B},\mathbf{T}_{\parallel})$, where p is the principal layer index, \mathbf{B} denotes the atom in the finite-sized unit cell corresponding to the p -th principal layer, and \mathbf{T}_{\parallel} is a two-dimensional translation vector such that $\mathbf{R}=\mathbf{B}+\mathbf{T}_{\parallel}$. Analogously, the structural constants can be transformed to the \mathbf{k} representation. Consequently, the physical Green's functions defined by Eqs. (9), (13), and (14), and the auxiliary Green's functions defined by Eqs. (28), (35), and (36) will have momentum index \mathbf{k} . Thus, the expression (17) for ASA charge density and expression (41) for current density should be transformed to

$$\rho_{\mathbf{R}}(r) = -i \frac{1}{8\pi^2} \frac{1}{N_{\parallel}} \sum_{\mathbf{k}} \sum_L \int dE G_{\mathbf{R}L,\mathbf{R}L}^<(\mathbf{k},E) [\phi_{\mathbf{R}}(r) + \dot{\phi}_{\mathbf{R}}(r)(E - E_{\nu,\mathbf{R}})]^2 \quad (46)$$

and

$$I = \frac{2e}{hA} \sum_{\mathbf{k}} \int dET(\mathbf{k},E,V) [f_{\mathcal{L}}(E) - f_{\mathcal{R}}(E)], \quad (47)$$

where expressions for $G_{\mathbf{R}L,\mathbf{R}L}^<(\mathbf{k},E)$ and $T(\mathbf{k},E,V)$ take the same form as in Eqs. (33) and (43) with the only difference that the structural constants and the auxiliary Green's functions will have momentum index \mathbf{k} . N_{\parallel} in Eq. (46) is the number of \mathbf{k} points in SBZ.

III. NUMERICAL PROCEDURE

The starting point of our implementation is a principal layers TB-LMTO-ASA code³⁷ that describes systems with two-dimensional translational symmetry in equilibrium at zero temperature. We present here a zero temperature *non-equilibrium* version of the code that assumes one and the same two-dimensional translational symmetry in each principal layer. Before starting the self-consistent calculation of the charge density in the central region, separate equilibrium self-consistent calculations for the leads are performed in a

bulk geometry. From these calculations the surface auxiliary Green's functions (35) and (36) and Γ^{α} matrices (34) are determined using a very effective decimation technique.⁴⁵

A. Energy integration

In order to calculate the radial charge density distribution in Eq. (46) one needs to calculate three energy moments of the lesser Green's function

$$M_{\mathbf{R}L}^n = \frac{-i}{N_{\parallel}} \sum_{\mathbf{k}} \int dE G_{\mathbf{R}L,\mathbf{R}L}^<(\mathbf{k},E) (E - E_{\nu,\mathbf{R}})^n, \quad (48)$$

where $n=0,1,2$. The energy integration in Eq. (48) is divided into integrations along two separate contours: from an energy E_B below the bottom of the valence band to $\mu_{\mathcal{L}}$ (equilibrium contour), and from $\mu_{\mathcal{L}}$ to $\mu_{\mathcal{R}}$ (nonequilibrium contour)

$$M_{\mathbf{R}L}^n = -\text{Im} \left\{ \frac{2}{N_{\parallel}} \sum_{\mathbf{k}} \int_{E_B}^{\mu_{\mathcal{L}}} dz G_{\mathbf{R}L,\mathbf{R}L}(\mathbf{k},z) (z - E_{\nu,\mathbf{R}})^n \right\} - \frac{i}{N_{\parallel}} \int_{\mu_{\mathcal{L}}}^{\mu_{\mathcal{R}}} dE G_{\mathbf{R}L,\mathbf{R}L}^{\mathcal{R}<}(\mathbf{k},E) (E - E_{\nu,\mathbf{R}})^n. \quad (49)$$

Here we used Eq. (37) and the fact that at zero temperature $f_{\mathcal{L}}(E)$ and $f_{\mathcal{R}}(E)$ are simple step functions. $G^{\mathcal{R}<}(E)$ is a part of $G^<(E)$ in Eq. (33) proportional to $f_{\mathcal{R}}(E)$. Expression (49) is valid for any sign of the applied potential. The first integrand on the right-hand side of Eq. (49) is an analytical function in the upper half plane of complex energy z . To avoid sharp features of the Green's function on the real axis, the integration is performed along the complex contour

$$z = (\mu_{\mathcal{L}} + E_B)/2 + [\cos \theta + i(1 - \varepsilon)\sin \theta](\mu_{\mathcal{L}} - E_B)/2, \quad (50)$$

where θ runs from $-\pi$ to 0. We found that the values of the moments (49) are not very sensitive to the eccentricity parameter ε of the contour. Typical ε in our calculations ranged from 0.3 to 0.5. Also we checked that the values of the moments do not depend on the choice of the energy E_B as long as it is below the bottom of the valence band, where the lesser Green's function $G_{\mathbf{R}L,\mathbf{R}L}(\mathbf{k},E)$ vanishes for all \mathbf{R} , L , and \mathbf{k} . The integral is evaluated by Gaussian quadrature with 10 to 20 points along the contour. In most cases, 14 points is enough for accurate evaluation of the integral.

The second integrand on the right-hand side of Eq. (49) is not an analytical function and has to be evaluated along the real axis. Two broadening parameters are used for evaluation of $G^{\mathcal{R}<}$. The first parameter δ is an imaginary part of energy $E_{\pm} = E \pm i\delta$ used to find the surface auxiliary Green's functions (35) and (36). The second parameter δ_2 is the imaginary part of energy $E_{\pm} = E \pm i\delta_2$ used to find auxiliary Green's functions of the central region g^{α} (28). The second broadening parameter δ_2 has to be set very small (typically $\delta_2 = 10^{-10}$ Ry) because broadening of g^{α} should be determined by the complex part of the surface self-energy matrices $\Gamma_{1,1}^{\alpha}$ and $\Gamma_{N,N}^{\alpha}$ and not by the complex part of the energy. In fact, if the contribution of δ_2 to the broadening of g^{α} becomes

comparable with the contribution from Γ^α factors, then formula (8) for the lesser Green's function is not longer valid. The δ_2 parameter is kept finite to avoid a false singularity at $\Delta + (\gamma - \alpha)(z - C) = 0$. The value of the parameter δ determines how many energy points are needed to evaluate the energy integral along the nonequilibrium contour. This integral is calculated using a trapezoidal method. In some cases the integrand has very sharp features, so care should be taken with respect to the broadening parameter δ and the number of energy points used along the nonequilibrium contour.

B. Electrostatic potential

The total potential is a sum of the LDA exchange-correlation potential and electrostatic potential. The later includes the Hartree potential and nuclei potentials. The electrostatic potential and charge distribution are determined self-consistently using an iteration scheme. A supercell is set up that includes the central region with layers $p=1, \dots, N$, two layers from the left lead $p=-1, 0$, and two layers from the right lead $p=N+1, N+2$. The atoms in the leads are assumed to have bulk charges and the atoms in the central region have charges determined in the previous iteration. The supercell is assumed to repeat itself in the xy plane (two translation vectors) and in the third direction (third translation vector), in such a way that atoms in principal layer -1 from the left lead become adjacent to atoms in principal layer $N+2$ from the right lead. In the case of leads of the same material the best choice of the third translation vector is when the coordinates of the atoms in principal layer -1 after translation coincide with coordinates of the atoms in principal layer $N+3$. The electrostatic potential in the center of the \mathbf{B} th sphere belonging to the supercell is determined by three-dimensional Ewald summation of Coulomb contributions from all spheres of the infinitely repeated supercell. The Ewald summation produces a periodic potential $\tilde{V}_{\mathbf{B}+\mathbf{T}} = \tilde{V}_{\mathbf{B}}$, where \mathbf{T} is a translation vector of the supercell. A linear contribution is added to the potential in order to satisfy the condition of potential drop V at the boundaries of the supercell. Thus, the electrostatic potential in the center of the \mathbf{B} th sphere reads

$$V_{\mathbf{B}} = \tilde{V}_{\mathbf{B}} + V \frac{z}{L_z} + C, \quad (51)$$

where L_z is the z component of the third translation vector of the supercell. The constant shift C is determined at the last stage of the iteration, when the charges are calculated, from the condition of charge neutrality of the central region (each principal layer in the lead regions is charge neutral already). The spherically symmetric electrostatic potential inside the \mathbf{B} th sphere is obtained from the radial charge distribution in this sphere by the solution of the radial Poisson's equation.

At the next step of the iteration the Schrödinger equation is solved to find the radial amplitudes $\phi_{\mathbf{R}l}(r)$ and $\dot{\phi}_{\mathbf{R}l}(r)$ for atoms in the central region. (Thus, in the LMTO approach, the basis functions (3) are updated on each iteration in accordance with the potential. This is different from other techniques that use fixed basis functions, optimized for the free

atom potentials.) Then, potential parameters for these atoms are calculated.⁴⁰ Using these potential parameters as well as structural constants in the maximally screened LMTO representation, the auxiliary Green's function and the lesser physical Green's function are calculated. Then $E_{\nu, \mathbf{R}l}$ is updated. It is chosen as a center of gravity of the $\mathbf{R}l$ projected density of states (DOS), from the condition

$$\sum_{m=-l}^l M_{\mathbf{R}l}^m = 0. \quad (52)$$

Finally, the energy moments and the radial density distributions are found. This completes the iteration. The described iteration cycle is repeated until input and output charge densities coincide with prescribed accuracy.

We checked how much the values of the electrostatic potentials and charges in the "bulk" principal layers $p=0$ and $p=N+1$ calculated using the above procedure for multilayer geometry differ from the corresponding values obtained by separate equilibrium bulk calculations for infinitely repeated leads (the bulk values were used for layers $p < 1$ and $p > N$ in actual multilayer calculations). If the difference was not small the size of the central region was increased. Additionally, we checked the convergence of the final results with respect to the size of the central region.

C. Test system

In order to test the method we perform calculations for a "capacitor" system of two gold (111) surfaces with a vacuum region between them. The central region of the system consists of four layers of gold atoms, three layers of empty spheres, and then again four layers of gold atoms. An empty sphere is a sphere which does not contain nuclear charge and represents vacuum regions in the ASA method. Semi-infinite gold right and left leads are assumed to be attached to the central region of the system. Positions and radii of all spheres correspond to bulk gold and the xy plane corresponds to the gold (111) surface. In the numerical implementation each principal layer consists of a single gold atomic sphere or an empty sphere. The self-consistent charge density and potential were calculated for this system in two different ways. First, we applied our *nonequilibrium* approach described above to the system with $V=1.36$ V applied bias (0.1 Ry). Then we applied the well-tested original *equilibrium* TB-LMTO-ASA method to the same system with a linear external potential that contains a 1.36 V discontinuity in the center of the vacuum region

$$V_{\text{ext}}(z) = \begin{cases} V(-z/L_z + 0.5), & z > 0 \\ V(-z/L_z - 0.5), & z < 0 \end{cases}. \quad (53)$$

The results for induced potential in the center of the spheres and induced charge on the spheres calculated by these two methods are shown in Fig. 1 for the central region with two additional principal layers from each lead (15 spheres total). Since the vacuum region is thick, there is essentially no current flowing through the system. Hence, the two methods produce essentially identical results. It is seen from the figure that the potential is very effectively screened by the first gold atoms adjacent to the vacuum region.

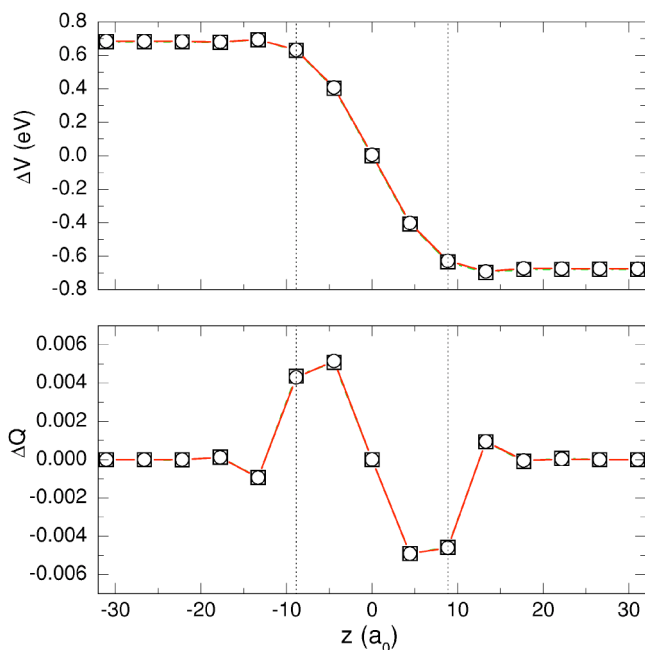


FIG. 1. (Color online) The difference between the electrostatic potential ΔV in the center of the spheres (top panel) and charges ΔQ on the spheres (bottom panel) for the “capacitor” with applied bias $V = -1.36$ V and with zero bias as a function of the sphere’s z coordinate (in units of Bohr radius a_0) calculated by the NEGF approach (circles) and by the equilibrium approach (squares). For the sake of comparison the potential of the equilibrium calculation is shown shifted by $+V/2$ for $z > 0$ and by $-V/2$ for $z < 0$. The circles are connected by solid lines and squares are connected by dashed lines. Vertical dotted lines show the positions of the left-most and right-most gold layers of the capacitor surfaces.

IV. APPLICATIONS

A. Benzene di-thiol molecule coupled to gold electrodes

The problem of understanding the contact resistance of a single molecule coupled to metallic electrodes has attracted great interest in recent years. A common way to attach a molecule to electrodes is by using thiol endgroups that easily bind to gold surfaces. A benzene di-thiol (BDT) molecule attached to gold (111) surfaces, one of the simplest systems of this type, has been studied experimentally^{47–49} and theoretically.^{3–5,9,11,13,16,20,26,50–54} There is no general agreement among theoretical groups or among experimental groups about the value of the small bias conductance for this system. Theoretical and experimental results for conductance of the system differ by more than two orders of magnitude, with theoretical results ranging from 0.1 to 32 μS , and experimental results ranging from 0.003 to 0.8 μS . The large spread in experimental results can be explained by the difficulty in controlling the exact geometry of the system. The theoretical results differ because different approximations are employed for the calculation. Di Ventra *et al.*⁵¹ employed a jellium approximation for the electrodes, while other groups^{3–5,9} used semi-empirical approaches to describe the electrodes. In Refs. 11,13,16,26 the electrodes were treated on the same footing as the molecule. Damle *et al.*¹⁶ and the TRANSIESTA group²⁶ used the NEGF formalism to calculate

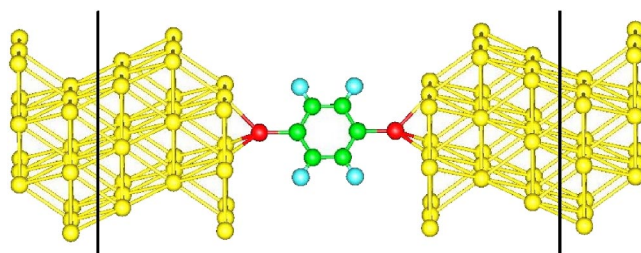


FIG. 2. (Color online) The computational cell used for simulation of transport properties of the BDT molecule coupled to two gold (111) surfaces. The cell repeats itself in the xy plane. Left and right semi-infinite gold leads are attached to the cell. The atoms between the two vertical lines constitute the central region, while all atoms in the figure form a supercell, periodic in three dimensions, used to calculate the electrostatic potential.

the current at finite bias, while Tomfohr and Sankey¹³ and Evers *et al.*¹¹ calculated the zero bias transmission. Importantly, all of these approaches employed the pseudopotential approximation to treat core electrons. Our approach differs from these calculations in that all electrons are treated, which allows, for example, a simple treatment of magnetic systems.³³ A further distinction is that the ASA-LMTO basis functions are constructed differently from the LCAO or Gaussian basis; for example, in the LMTO approach the basis functions are updated at each iteration following the change in the potential, while in other approaches they are fixed and optimized for the description of free atoms. Another distinction is that our LMTO basis functions are long ranged, while LCAO and Gaussian functions are localized.

In this section we apply our method to calculate the electronic structure and transport characteristics of the BDT molecule coupled to two Au(111) surfaces. Recently, several theoretical studies have shown^{9,13,51–54} that the conductance of the benzene di-thiol molecule strongly depends on the geometry how the molecule is positioned with respect to the gold electrodes. Moreover, the precise geometry of the system is not known in the experiment. Thus, we may only quantitatively compare the results of different theoretical approaches obtained for the same geometry. The geometry of the system that we study is shown in Fig. 2. The central region of the system consists of three Au(111)-(3×3) layers, the layer with the BDT molecule, and then three more Au(111)-(3×3) layers, positioned symmetrically to the first three Au layers. The semi-infinite left and right gold electrodes are attached to the ends of the central region. The cell is assumed to repeat itself periodically in the xy plane. Atomic positions were determined as follows. First, we find the Au-S distance by positioning a single S atom over the Au(111) surface at a threefold site and then relax the positions of the atoms by using the VASP molecular dynamics program⁵⁵ with LDA exchange-correlation potential. Then we placed the BDT molecule between the gold surfaces with the calculated Au-S distance and relaxed the structure again with fixed dimensions of the unit cell. In this procedure we obtained a Au-S distance of 2.42 Å and a S-C distance of 1.74 Å, in agreement with the values obtained in Ref. 26. We checked that our results do not change significantly if we choose relaxed Au positions or ideal bulk positions of Au, thus confirming

the result of the TRANSIESTA group.²⁶ Also we checked that variation of the atomic positions of the gold atoms or atoms of the benzene di-thiol molecule within 0.03 Å range do not affect our results significantly.

In our calculations we neglected the electron-phonon coupling effects and changes of the atomic positions due to the current-induced forces. It has been shown recently⁵⁶ that the current-induced forces do not substantially affect the value of the current for biases as high as 5 V. The electron-phonon coupling effects were also estimated to be small,⁵⁷ at least for biases up to 0.1 V. Also we checked the effect of increasing the cell size. We performed calculations for a Au(111)-(4 × 4) system and found that increasing the *x-y* cell size from (3 × 3) to (4 × 4) has only minor effects on the equilibrium DOS and transmission spectrum.

The other source of error in our approach is the use of the local density approximation to describe a many-body system. It is well known that LDA suffers from many deficiencies, in particular its underestimate of band gaps in semiconductors and insulators. The error in the determination of the molecule energy levels may affect the position of the resonant peaks in the DOS and transmission function and hence the magnitude of the current. The natural way to go beyond LDA is to perform calculations within the so-called GW approximation of the many-body theory. It has been shown recently that the GW approximation can accurately predict electronic structure and band gaps even for strongly correlated systems.⁵⁸ Unfortunately, the GW calculations are very time consuming and cannot be performed, at least for now, with the large number of atoms required for the present calculations.

The atomic sphere approximation assumes that all space is filled by (overlapping) spheres and that the volume of the interstitial region vanishes. In order to fill the vacuum space between Au electrodes with spheres, we used the Stuttgart LMTO-ASA program.⁵⁹ This program fills space by empty spheres using the following criteria: The sum of the volume of all spheres should be equal to the volume of all space, the average overlap between the spheres should be minimal, and the radii of all spheres should be chosen in such a way that the spheres overlap in the region close to the local maximum of the electrostatic potential. The choice of the empty spheres packing structure is not unique. This is the main drawback of ASA when applied to systems that contain large vacuum regions. On the other hand, for a large enough number of closely packed empty spheres the results only weakly depend on the empty spheres packing structure. In our case we used 139 empty spheres to fill the vacuum space in the central region in addition to 54 Au atomic spheres and 12 BDT atomic spheres. In order to verify that this number of empty spheres is sufficient for an accurate description of the electronic structure of the system we performed full potential calculations³⁸ for a supercell with three-dimensional periodicity containing the BDT molecule and from four to five Au(111)-(3 × 3) layers. The results for the density of states projected on the BDT molecule atomic spheres obtained by full-potential supercell calculations and by LMTO-ASA calculations for an equilibrium system in the multilayer geometry are shown in Fig 3. It is seen from the figure that these two methods produce similar results for the DOS, confirming the appropriateness of the empty sphere packing structure.

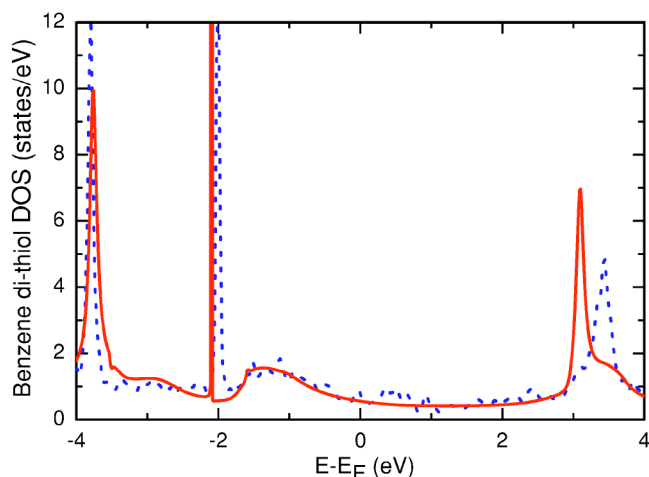


FIG. 3. (Color online) The density of states projected on the BDT molecule atomic spheres obtained by the LMTO-ASA method (solid line) for an equilibrium system in the multilayer geometry and by full potential supercell calculations (dotted line).

The general shape of the molecule-projected DOS in Fig. 3, the position of the maximum of the broad peak at about -1.3 eV as well as the 5.2 eV difference in positions of the two sharp peaks at -2.1 and $+3.1$ eV agree well with results obtained by the TRANSIESTA group,²⁶ although the positions of the last two peaks are shifted to lower energies by about 0.3 eV compared to our results. Also, our DOS does not show the fine structure between peaks at -2.1 and -1.3 eV that can be found in the TRANSIESTA results. The DOS projected on the BDT molecule found in Ref. 3 differs somewhat with our results and with the results presented in Ref. 26. Note that the authors of Ref. 3 used a system setup of a single BDT molecule on the surface of gold electrodes with a finite number of atoms in the *xy* plane, while our calculation and Ref. 26 use a system setup of a self-assembled monolayer with (3×3) periodicity in the *xy* plane. Also, the authors of Ref. 26 used only one $\mathbf{k}=0$ point in the SBZ to reduce the computational efforts,¹⁹ while we use a $n \times n$ grid in the SBZ, where n is the number of \mathbf{k} points along each translation vector of SBZ. Our results are well converged for $n=10$, giving 36 irreducible \mathbf{k} points in the SBZ. We found that the use of just one $k=0$ point in SBZ is not sufficient to obtain accurate DOS and transmission function, although, because of the large size of the unit cell in the *x-y* plane, the dependence on the number of \mathbf{k} points is weak and results begin to converge already for $n \sim 5$.

It is interesting to see how the DOS changes if a finite bias is applied to the leads. Figure 4 shows the DOS projected on the left and right sulfur atomic spheres for four different applied voltages. The figure shows that the sulfur peaks in the DOS move symmetrically, relative to the average chemical potential $(\mu_R + \mu_L)/2$, essentially following the left and right Fermi levels. Indeed, the difference between the positions of the peaks for the left and right sulfur DOS corresponds to the value of the applied bias multiplied roughly by a factor of 0.85. It can be concluded that the energy levels of the Kohn-Sham wave functions that are spatially concentrated inside a sulfur atomic sphere, essentially

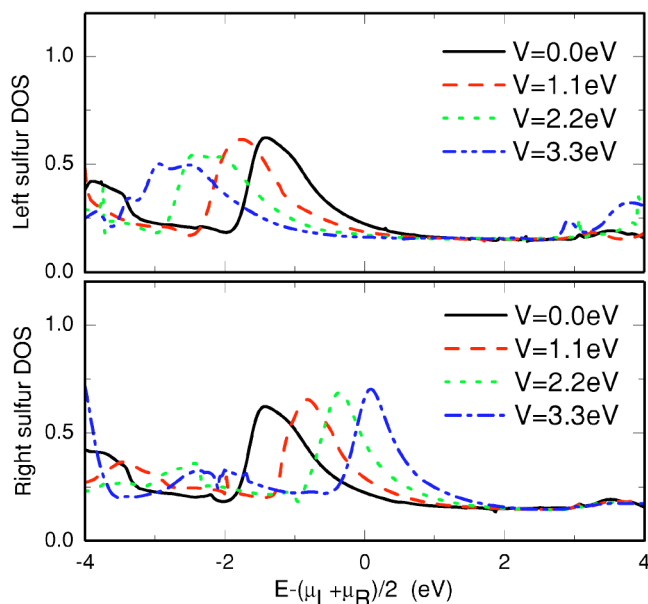


FIG. 4. (Color online) DOS projected on the left (top panel) and right (bottom panel) sulfur atomic sphere for four different bias voltages.

follow the chemical potential of the gold electrode adjacent to that sulfur atom.

The DOS projected on the left-most and right-most carbon atomic spheres are shown in Fig. 5. One can see that the outer carbon DOS changes only weakly with applied bias. The small changes in DOS around the peak at -2.1 eV correspond to the contribution of long-ranged wave functions that respond to the change in the chemical potentials of the leads. Figure 6 shows the DOS projected on the four inner

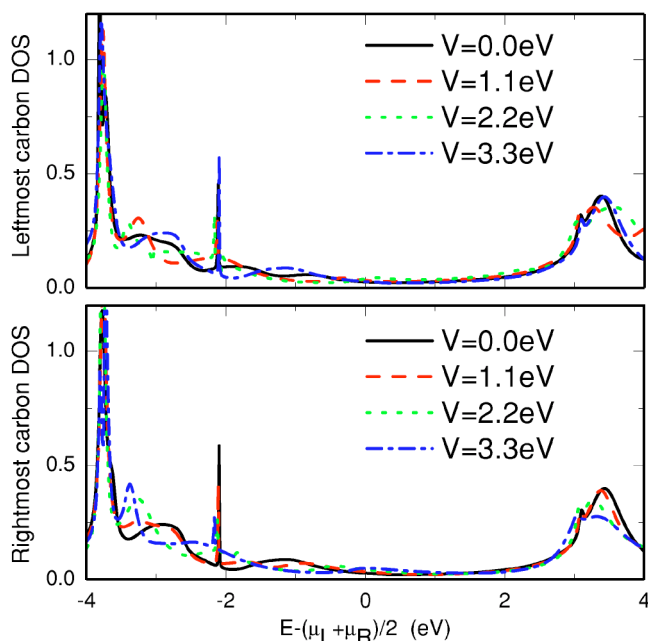


FIG. 5. (Color online) DOS projected on the left-most (top panel) and right-most (bottom panel) carbon atomic sphere for four different bias voltages.

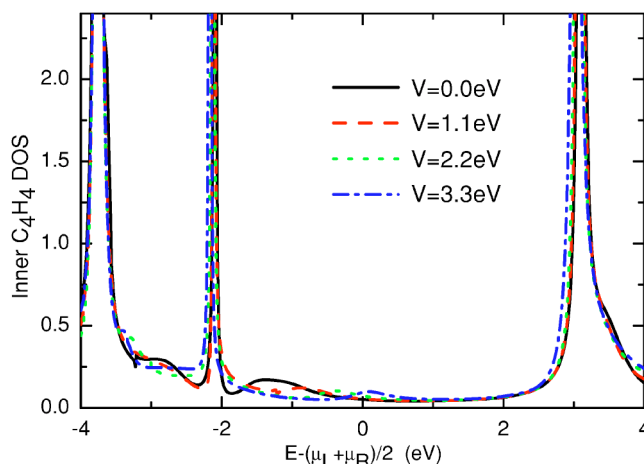


FIG. 6. (Color online) DOS projected on the C_4H_4 inner atoms of the BDT molecule for four different bias voltages.

carbon spheres and four hydrogen spheres. The DOS of the inner C_4H_4 atoms is almost unaffected by applied bias. The small changes in DOS around the peak at -2.1 eV for *eight* atomic spheres in Fig. 6 are about the same order of magnitude as those for the *single* right-most or left-most carbon sphere in Fig. 5. Thus, the applied bias affects mostly the states with wave functions concentrated in the sulfur spheres by shifting the energy levels of these states close to the chemical potential of the nearest electrode. Analyzing Figs. 4–6, we can clearly identify the origin of the peaks in the zero-bias molecule-projected DOS shown in Fig. 3. The broad peak at -1.3 eV corresponds to the Kohn-Sham wave functions that are mostly concentrated inside sulfur atomic spheres and have small weight inside other atomic spheres of the BDT molecule. The three narrow peaks at -3.8 , -2.1 , and 3.1 eV correspond to the wave functions distributed over the inner ring of six carbon and four hydrogen atomic spheres with smaller weight inside the sulfur spheres.

The induced potential ΔV , defined as the difference between the electrostatic potential in the center of a sphere for the system with an applied bias of 2.72 V and that for the system with zero bias, is shown in Fig. 7 as a function of the z coordinate of the sphere’s center. The induced potential is basically a smooth function of the coordinate z , with an almost linear behavior in the molecule region. Two small kinks at $z = \pm 5.87 a_0$ correspond to the sulfur spheres. These kinks in the potential can be explained by the fact that the induced charge on a sulfur sphere is more than two times larger than induced charges on neighboring spheres.

It can be seen from Fig. 7 that the induced potential is well screened beyond the second Au layer ($z = \pm 13.28 a_0$), thus supporting our choice for the central region. We also confirmed that results do not change significantly if a larger number of Au layers are included in the central region. The difference between the values of the electrostatic potential near the left and right sulfur spheres is about equal to the applied bias multiplied by a factor of 0.85 . This explains the value of the shift of the sulfur DOS in Fig 4. The very small dependence on the applied bias of the DOS projected on the carbon and hydrogen atoms (see Figs. 5 and 6) can be explained by the fact that the wave functions of the inner ring

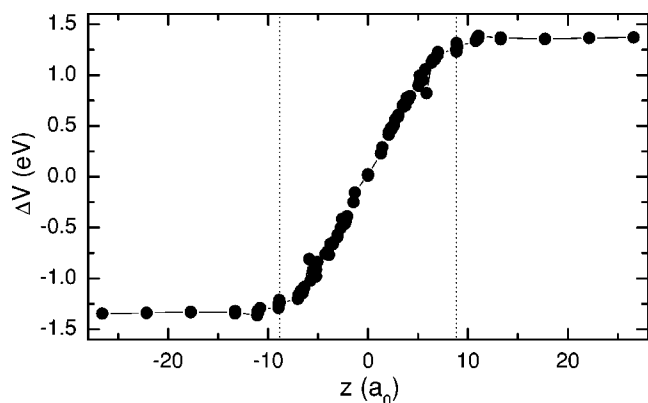


FIG. 7. The Induced potential at the sphere centers as a function of the sphere's z coordinate for the system of BDT molecules attached to two (111) gold electrodes with an applied bias of 2.72 V. The induced potential for 241 spheres is shown, including 139 empty spheres, 12 BDT spheres, 54 Au spheres in the central region, and an additional 36 Au spheres in the two left lead layers and two right lead layers that are included in the construction of the supercell for electrostatic potential calculation. The atomic spheres that have the same values of the z -coordinate and induced potential value are shown in the figure as a single point. Vertical dotted lines show the positions of the left-most and right-most gold layers of the right and left electrode, respectively.

of the BDT molecule are distributed over the whole ring and have symmetry with respect to inversion of the z coordinate. Treating the induced potential, antisymmetric with respect to inversion of the z coordinate, as a small perturbation, the correction to the energy level of such wave functions in first-order perturbation theory vanishes. This symmetry argument does not apply to the *degenerate* equilibrium states concentrated mostly inside the left and right sulfur atomic spheres and whose energy levels follow the induced potential.

The current as a function of applied bias is shown in Fig. 8. For comparison we also show the current calculated by using the zero-bias transmission function $T(k, E, V=0)$ in Eq.

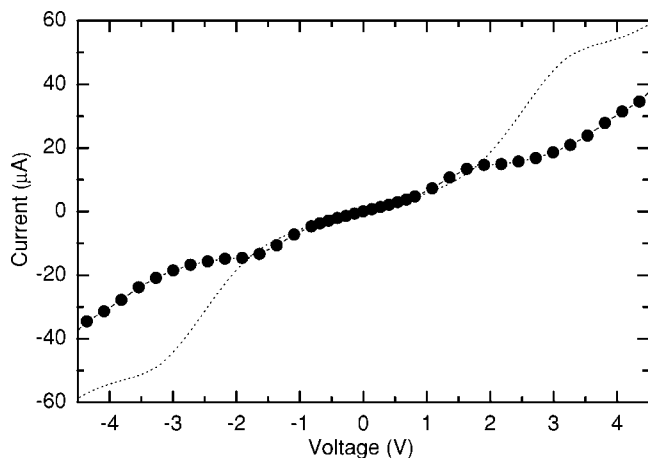


FIG. 8. Current as a function of bias. Solid line with dots represents current obtained by the NEGF approach. Dashed line represents current calculated from zero-bias transmission coefficient (see text for details).

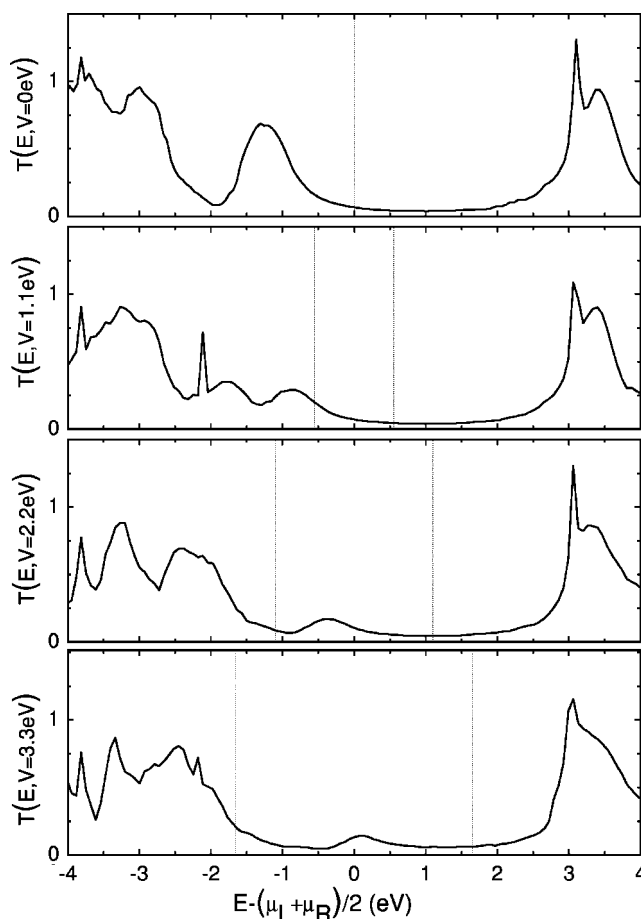


FIG. 9. Transmission coefficient calculated by the NEGF approach for four different bias voltages. The bias window is shown with the vertical dotted lines.

(47). It is seen that the currents obtained by these two methods coincide only for small bias; for voltage larger than 2 V they significantly deviate. Thus, the nonequilibrium effects become essential for transport properties of the system for biases larger than 2 V. In order to better understand the dependence of the current on applied bias we present in Fig. 9 the transmission spectrum calculated by the NEGF approach for four different bias voltages. The bias window, corresponding to μ_R and μ_L , is shown in the figure by vertical dotted lines. At zero bias the peaks in the transmission function correspond to the peaks of the DOS (see Fig. 3) except that the narrow DOS peak at -2.1 eV is not present in the zero-bias transmission. This may be explained by the fact that the very narrow peak of the DOS at -2.1 eV corresponds to a localized molecule state which has weak coupling to the gold leads. The broad sulfur peak 1.3 eV below the Fermi energy determines the value of the zero-bias conductance.

The zero-bias transmission spectrum presented in the top panel in Fig. 9 is in rough agreement with the transmission spectrum obtained by Xue *et al.*,³ and Xue and Ratner,⁹ by Evers *et al.*,¹¹ and by TRANSIESTA.²⁶ In particular, all four methods show that the transmission peak closest to the Fermi energy is located about 1.3 eV below the Fermi energy. This result is in disagreement with results of Di Ventra *et al.*,⁵¹

who found that the Fermi energy is closer to the LUMO transmission peak.

The zero-bias conductance is proportional to the transmission coefficient at the Fermi energy, as given by Eq. (44). We obtain a value for the zero-bias conductance of $5.0 \mu\text{S}$. Di Ventra *et al.*⁵¹ found a conductance of $3 \mu\text{S}$. Xu *et al.* found a conductance of $2.8 \mu\text{S}$,³ and later corrected it to $4.8 \mu\text{S}$.⁹ Evers *et al.*¹¹ obtain the value of $12 \mu\text{S}$, Tomfohr and Sankey¹³ found the value of $7 \mu\text{S}$, and Damle *et al.*¹⁶ found the value of $6 \mu\text{S}$. The TRANSIESTA group obtained a conductance value of $32 \mu\text{S}$. Such a large conductance arises because the transmission peak at -1.3 eV obtained in Ref. 26 is twice as broad as the zero-bias transmission peak shown in Fig. 9.

The experimental value of the zero-bias conductance was measured as $0.003 \mu\text{S}$ in earlier work by Reed *et al.*⁴⁷ In more recent experiments,⁴⁹ this value was measured to be more than two orders of magnitude larger, namely, $0.85 \mu\text{S}$. This large difference in experimental results may be explained by the fact that the exact geometry of the system cannot be controlled when measurements of the conductance are made.

It is interesting to see how the transmission spectrum calculated by the NEGF approach changes with bias. The peak in the zero-bias transmission at -1.3 eV splits into two peaks that move away from each other as the bias increases, in accordance with splitting of the left and right sulfur projected DOS (see Fig. 4). The maximum of the “right sulfur” transmission peak that moves to higher energy decreases with bias. It can be explained by the fact that for finite bias the energy of an electron propagating from right to left cannot be simultaneously a resonant energy of both left and right sulfur projected DOS as it happens at zero bias. The maximum of the “left sulfur” transmission peak that moves to lower energies decreases for applied bias less than $\sim 1 \text{ V}$ but after this it begins to increase because it becomes resonant with the energy levels of the inner ring of the BDT molecule. The peak of the transmission spectrum at 3 eV is not changed much with applied bias, in accordance with the behavior of the inner ring projected DOS (see Fig. 6).

We can now explain the behavior of the current as function of applied bias shown in Fig. 8. At first ($V \leq 1.4 \text{ V}$), the current increases supralinearly, as the width of the Fermi-level window increases and the left Fermi level rides up the peak of the right sulfur. Current saturation (at $\sim 1.6 \text{ V}$) arises as the maximum of the right sulfur transmission peak reaches the left Fermi level. Around a bias of 3 V the current increases again because the bias window approaches the next resonance peak of the transmission spectrum at lower energy. This pattern of current behavior is in agreement with previous results,^{9,13,26} with the saturation plateau in the same voltage range of $1.6\text{--}3 \text{ V}$. No plateau appears in the I - V curve obtained by Damle *et al.*¹⁶ The magnitude of the current at the plateau is roughly the same in our work and in Refs. 9,13, but half as much as in Ref. 26. The current measured in recent experimental work⁴⁹ shows supralinear current increase (for measured voltages up to 0.7 V), although the magnitude of the current is six times less than our theoretical simulations.

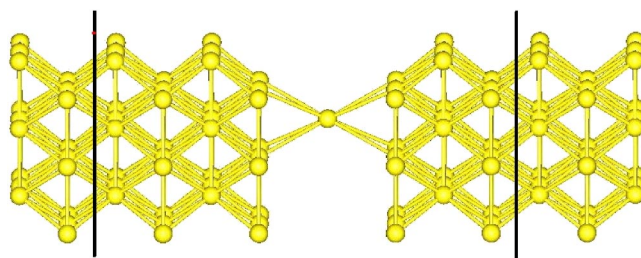


FIG. 10. (Color online) The computational cell used for simulation of transport properties of a single Au (Pt) atom coupled to two Au (Pt) surfaces. The cell repeats itself in the xy plane. Left and right semi-infinite leads are attached to the cell. The atoms between the two vertical lines constitute the central region, while all atoms in the figure form a supercell, periodic in three dimensions, used to calculate the electrostatic potential.

B. Contact resistance of a single Au (Pt) atom coupled to Au (Pt) electrodes

Atomic-sized contacts (ASCs) have been intensively studied both experimentally and theoretically (for a review on ASCs see Ref. 60). It is known that the conductance of certain materials (such as alkaline or noble metals) takes an integer value of the quantum of conductance $G_0 = 2e^2/h$ when the size of the contact becomes comparable with the Fermi wavelength. The experimental studies show that the conductance of a single Au atom is distributed in a narrow range near G_0 ,^{25,61–64} while the conductance of a single Pt atom varies in a much broader range of $1.5\text{--}2.0G_0$.^{25,63,65} The first *ab initio* calculation of the contact resistance and I - V curve of a single Au (Pt) atom coupled to Au (Pt) electrodes was presented²⁵ by the TRANSIESTA group. In this section we apply our method to calculation of the I - V -curves of single Au and Pt atoms and compare our results with TRANSIESTA results and experiment.

The atomic structure of the system is shown in Fig. 10. The central region of the system consists of four $M(100)$ - (3×3) layers with atoms in ideal bulk positions, the layer with a single M atom (the central atom), and four more $M(100)$ - (3×3) layers, positioned symmetrically to the first four M layers. Here M denotes the metal, Au or Pt. The atom-electrode distance was chosen to be 2.9 \AA , the same as in Ref. 25. The semi-infinite left and right M electrodes are attached to the ends of the central region. The cell is repeated periodically in the xy plane.

The zero bias transmission spectrum for three empty spheres packing structures of the gold system with 83, 87, and 95 empty spheres is presented in Fig. 11. The transmission curves are very similar for these packing structures, thus, the convergence with respect to the number of empty spheres is achieved. In order to better understand the equilibrium transmission spectrum shown in Fig. 11 we present the spd angular momentum resolved DOS projected on the central Au atomic sphere in Fig. 12. It is easy to see the correspondence between the peaks of the DOS for different angular momentum projections and the peaks of the transmission spectrum in Fig. 11. The main contribution to the DOS of the central gold atom near the Fermi energy comes from a broad s -character peak. The broad peak with the same

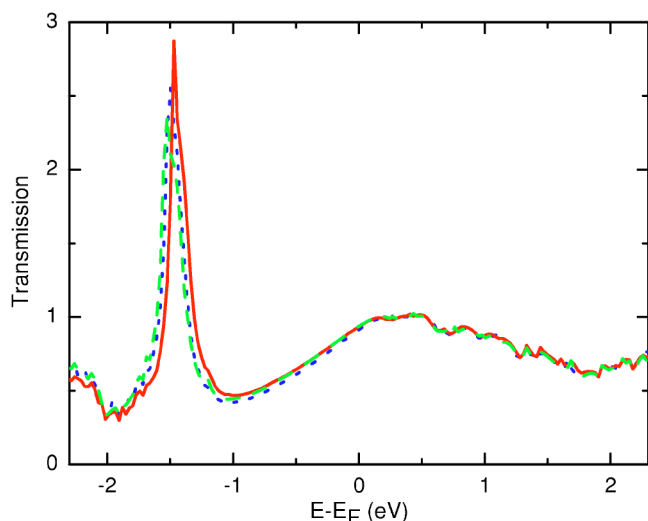


FIG. 11. (Color online) Zero-bias transmission spectrum for a single Au atom coupled to semi-infinite Au electrodes for different empty spheres packing structures, with 83 (solid line), 87 (dashed line), and 95 (dotted line) empty spheres.

shape can be seen in the transmission curves in Fig. 11. It can be concluded that the wave functions with *s*-like character give most of the contribution to the zero bias transmission near the Fermi energy, and, correspondingly, to the conductance. Our value of $0.94G_0$ for the zero-bias conductance of a single gold atom coupled to Au electrodes is in good agreement with the TRANSIESTA value of $1.05G_0$ (Ref. 25) and the experimental results.^{25,61–64}

The transmission spectra calculated for the system at zero bias and under an applied bias of 1.09 V are shown in Fig. 13. The curves are very similar over a wide range of energy. Such a weak dependence of the transmission on the energy and applied bias for the gold system results in almost ohmic behavior of the current, shown in Fig. 14, with respect to the applied voltage. Only small deviations from linear behavior

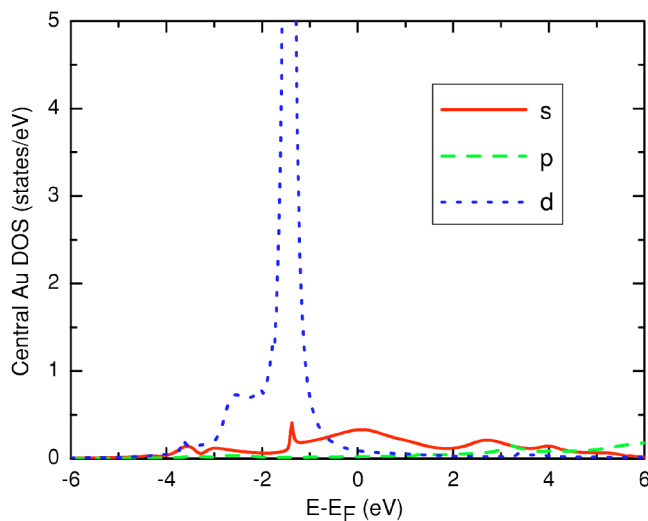


FIG. 12. (Color online) The *spd* angular momentum resolved DOS projected on the central gold atomic sphere for the single gold atom system.

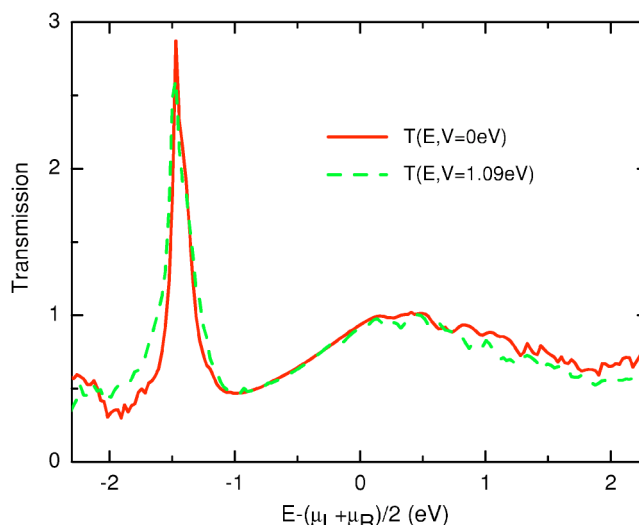


FIG. 13. (Color online) Transmission spectrum for a single Au atom coupled to semi-infinite Au electrodes calculated at zero bias and at a bias of 1.09 V.

occur at higher voltages for the gold system. Figure 14 also shows the current calculated from the zero-bias transmission spectrum by using $T(\mathbf{k}, E, V=0)$ in Eq. (47), which almost coincides with the current obtained by self-consistent calculations with finite applied bias. This is consistent with the transmission spectrum being weakly dependent on the applied bias. The transmission spectrum at zero bias and finite bias shown in Fig. 13 agrees well with TRANSIESTA results.²⁵

We now turn to the system of a single Pt atom coupled to two Pt electrodes. The zero bias transmission spectrum for three empty spheres packing structures of the system with 83, 91, and 107 empty spheres are shown in Fig. 15. The transmission curves are very similar for these packing struc-

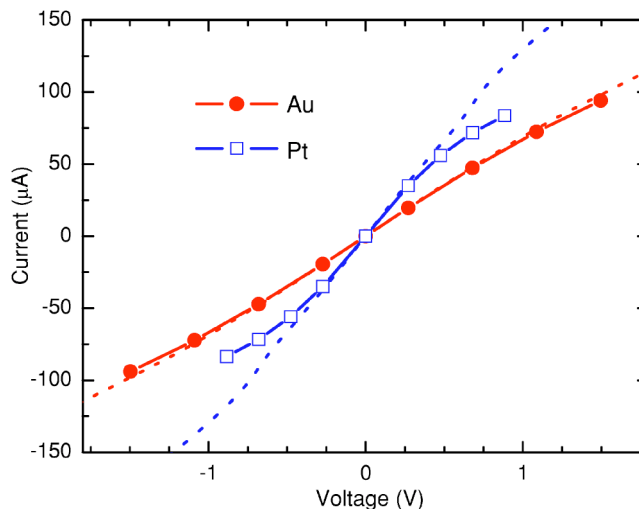


FIG. 14. (Color online) Current as a function of applied voltage for the gold system (solid line with filled circles) and platinum system (solid line with open squares). The currents for these two systems calculated from the zero bias transmission spectrum are also shown by dotted lines that coincide at small voltage with appropriate solid lines.

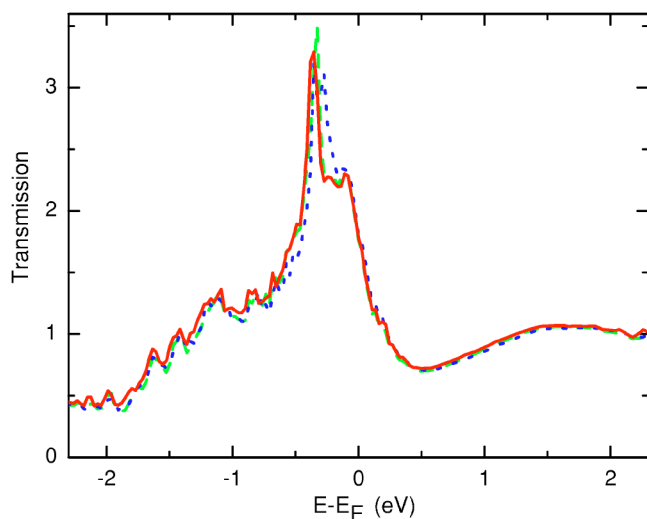


FIG. 15. (Color online) Zero-bias transmission spectrum for a single Pt atom coupled to semi-infinite Pt electrodes for different empty spheres packing structures, with 83 (solid line), 91 (dashed line), and 107 (dotted line) empty spheres.

tures; thus, the convergence with respect to the number of empty spheres is achieved. Figure 16 shows the *spd* angular momentum resolved DOS projected on the central Pt atomic sphere. Unlike gold, platinum has an open *d* shell, so there is significant *d* character contribution to the DOS of the central Pt atom near the Fermi energy. It is easy to see the correspondence between the *d*-character peak at -0.3 eV, broader than the *s*-character peak at $+1.7$ eV of the momentum resolved DOS in Fig. 16 and the peaks of the transmission spectrum in Fig. 15. Thus, wave functions with both *s* and *d* characters contribute to the zero bias transmission near the Fermi energy with somewhat larger contributions of the *d*-character wave functions. Our value of $1.76G_0$ for zero-bias conductance of a single Pt atom coupled to Pt electrodes is in good agreement with the TRANSIESTA value of $1.73G_0$ (Ref. 25) and the experimental results.^{25,63,65}

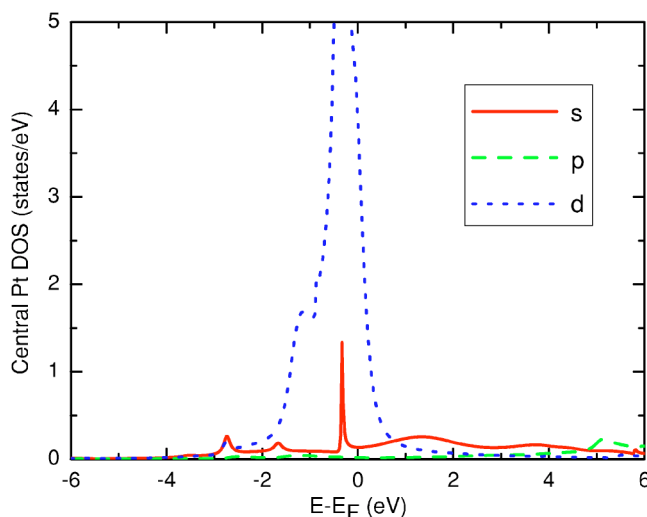


FIG. 16. (Color online) The *spd* angular momentum resolved DOS projected on the central platinum atomic sphere for the single platinum atom system.

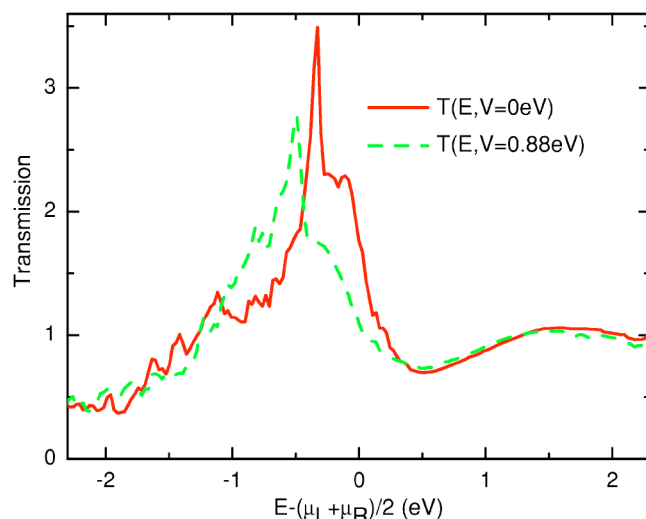


FIG. 17. (Color online) Transmission spectrum for a single Pt atom coupled to semi-infinite Pt electrodes calculated at zero bias and at a bias of 0.88 V.

The transmission spectrum calculated for the system under zero bias and under an applied bias of 0.88 V are shown in Fig. 17. These curves significantly deviate at energies less than 0.5 eV. The strong dependence of the transmission on the energy and applied bias for the platinum system results in a much stronger deviation of the *I-V* curve, shown in Fig. 14, from linear behavior as compared to the *I-V* curve for the gold system. The peak of the transmission function at -0.3 eV shifts to lower energies with applied bias and its value decreases. This results in a reduction of the current compared to the current calculated from the zero-bias transmission spectrum shown by a dotted line in Eq. (47). Our results agree with experiential and theoretical results presented in Ref. 25.

The induced potentials for the gold and platinum systems with applied bias of 0.68 V are shown in Fig. 18. As can be seen, the induced potentials for the gold and platinum systems are very similar. Most of the potential drop occurs between surface layers of the electrodes, shown in the figure by dotted lines. Between these lines the voltage drop is almost linear. Because of the small size of the vacuum region the four Au(Pt) layers to the left and to the right of the central atom are not enough to completely screen the potential. Some small voltage drop at the end of the supercell can still be seen in Fig. 18. In order to quantify the importance of this effect, we performed calculations with five Au(Pt) layers to the left and right of the central Au(Pt) atom. The effect of the increased size of the central region on the conductance values was within our numerical accuracy of $0.01G_0$.

V. CONCLUSION

This paper described an *ab initio* method and its implementation for the calculation of the electronic structure and transport properties of a nanoscale system coupled to electrodes with applied bias voltage. The method is based on a nonequilibrium Green's function approach using an all-

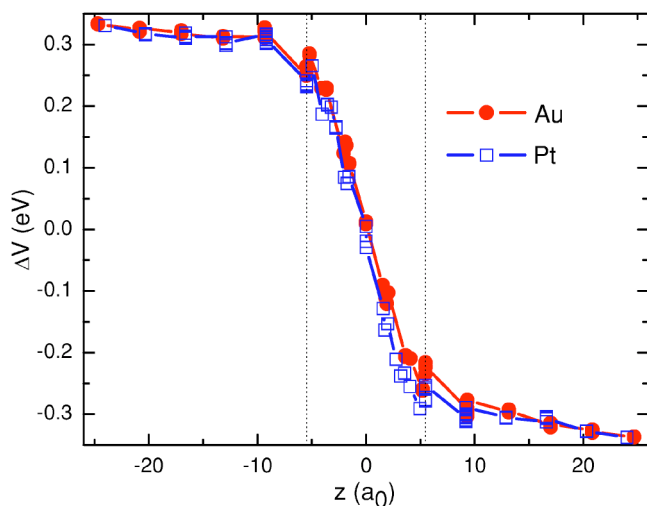


FIG. 18. (Color online) The induced potential in the center of spheres as a function of the sphere's z coordinate for the gold system (solid line with filled circles) and the platinum system (solid line with open squares). In both cases the bias voltage equals 0.68 V. The induced potential is shown for all atomic and empty spheres of the central region and for the additional 36 spheres of two left lead layers and two right lead layers that are included in the construction of the supercell for the electrostatic potential calculation. Vertical dotted lines show the positions of the left-most and right-most Au(Pt) layers of the right and left electrode, respectively.

electron TB-LMTO-ASA formalism, and can be applied to a variety of systems, as illustrated by calculations for single molecules and single-atom contacts.

While a significant fraction of this paper is devoted to the technique, the calculations presented for the BDT molecule show that even simple-looking current-voltage curves can have interesting physical origins. Indeed, for the BDT molecule connected to gold electrodes, the physical picture that emerges is (1) electric fields are screened within the first two gold layers; (2) the voltage drop is linear across the molecule; (3) the end sulfur atoms are strongly coupled to the electrodes, while the central part of the molecule is weakly coupled; (4) electron transmission occurs through wave functions that are localized on the end sulfur atoms, with the zero-bias Fermi level near and above these states; and (5) applied bias splits the degeneracy of these states, and leads to a nonlinear increase of the current with bias.

Finally, we note that a meaningful comparison between experiment and theory first requires agreement between the various experiments and between the different theoretical approaches. For single atom contacts, our results are in excellent agreement with previous calculations, and seem to agree with experiment. For BDT, at this time, neither experiments nor theory have converged to a consensus on the behavior of this molecule. As theoretical approaches have progressed, various approximations have been removed, most notably in the present work the pseudopotential approximation. As we hope to remove the ASA by implementing a full-potential version of the method presented here, we expect that a converged theoretical answer for the behavior of molecular systems within the LDA will soon be available.

ACKNOWLEDGMENT

Sandia is a multiprogram laboratory operated by Sandia Corporation, a Lockheed Martin Company, for the United States Department of Energy under Contract No. DE-AC04-94-AL85000.

APPENDIX A

In this Appendix we will rewrite Eq. (6) for the charge density in terms of site-diagonal elements of lesser Green's functions, thus making the equation much more suitable for numerical implementation. Let index \mathbf{R}_0 denote a sphere which contains vector \mathbf{r} , where we calculate the charge density. Let us increase, for a moment, the width of the central region in such a way that the distance between the sphere \mathbf{R}_0 and any sphere \mathbf{R} belonging to the left or right lead is large enough, so the coefficients $h_{\mathbf{R}_0,\mathbf{R}}$ of the LMTO tail in the Eq. (3) vanish (in this Appendix we will omit the angular momentum indices for brevity). In other words, we assume that all LMTO's used in the summations over \mathbf{R} and \mathbf{R}' in Eq. (6) have heads at atoms that belong only to the central region, and the tails of LMTO's with heads at atoms in the lead regions vanish for a given sphere \mathbf{R}_0 . Thus, we may apply the formula (8) for the lesser Green's function in the central region to Eq. (6), because contributions from sites \mathbf{R} or \mathbf{R}' belonging to leads vanish. Let us consider a product

$$\begin{aligned} & \sum_{\mathbf{R},\mathbf{R}'} \chi_{\mathbf{R}}(\mathbf{r}) G_{\mathbf{R},\mathbf{R}'}(E) H_{\mathbf{R}',\mathbf{R}_l} \\ &= \sum_{\mathbf{R}'} \phi_{\mathbf{R}_0}(\mathbf{r}_{R_0}) G_{\mathbf{R}_0,\mathbf{R}'}(E) H_{\mathbf{R}',\mathbf{R}_l} \\ &+ \sum_{\mathbf{R},\mathbf{R}'} \dot{\phi}_{\mathbf{R}_0}(\mathbf{r}_{R_0}) h_{\mathbf{R}_0,\mathbf{R}} G_{\mathbf{R},\mathbf{R}'}(E) H_{\mathbf{R}',\mathbf{R}_l}, \end{aligned} \quad (\text{A1})$$

where \mathbf{R}_l denotes a site belonging to the left or right lead. Such products appear in the expression for $\chi_{\mathbf{R}}(\mathbf{r}) G_{\mathbf{R},\mathbf{R}'}^<$ in Eq. (6) if we apply definitions (10)–(12) to the expression for the lesser Green's function (8). The last term in the right hand side of Eq. (A1) can be rewritten by using relation (5) and definition of the Green's function (9)

$$\begin{aligned} & \sum_{\mathbf{R},\mathbf{R}'} \dot{\phi}_{\mathbf{R}_0}(\mathbf{r}_{R_0}) h_{\mathbf{R}_0,\mathbf{R}} G_{\mathbf{R},\mathbf{R}'}(E) H_{\mathbf{R}',\mathbf{R}_l} \\ &= \sum_{\mathbf{R},\mathbf{R}'} \dot{\phi}_{\mathbf{R}_0}(\mathbf{r}_{R_0}) H_{\mathbf{R}_0,\mathbf{R}} G_{\mathbf{R},\mathbf{R}'}(E) H_{\mathbf{R}',\mathbf{R}_l} \\ &- \sum_{\mathbf{R}'} \dot{\phi}_{\mathbf{R}_0}(\mathbf{r}_{R_0}) E_{\nu,\mathbf{R}_0} G_{\mathbf{R}_0,\mathbf{R}'}(E) H_{\mathbf{R}',\mathbf{R}_l} \\ &= \sum_{\mathbf{R}'} \dot{\phi}_{\mathbf{R}_0}(\mathbf{r}_{R_0}) E G_{\mathbf{R}_0,\mathbf{R}'}(E) H_{\mathbf{R}',\mathbf{R}_l} - \dot{\phi}_{\mathbf{R}}(\mathbf{r}_{R_0}) H_{\mathbf{R}_0,\mathbf{R}_l} \\ &- \sum_{\mathbf{R}'} \dot{\phi}_{\mathbf{R}_0}(\mathbf{r}_{R_0}) E_{\nu,\mathbf{R}_0} G_{\mathbf{R}_0,\mathbf{R}'}(E) H_{\mathbf{R}',\mathbf{R}_l} \\ &= \sum_{\mathbf{R}'} \dot{\phi}_{\mathbf{R}_0}(\mathbf{r}_{R_0}) (E - E_{\nu,\mathbf{R}_0}) G_{\mathbf{R}_0,\mathbf{R}'}(E) H_{\mathbf{R}',\mathbf{R}_l}. \end{aligned} \quad (\text{A2})$$

In the last line of Eq. (A2) we used the fact that the Hamil-

tonian matrix elements $H_{\mathbf{R}_0, \mathbf{R}_l}$ are related to the coefficients $h_{\mathbf{R}_0, \mathbf{R}_l}$ by Eq. (5) and vanish by our assumption. Thus, the product (A1) takes the form

$$\begin{aligned} & \sum_{\mathbf{R}, \mathbf{R}'} \chi_{\mathbf{R}}(\mathbf{r}) G_{\mathbf{R}, \mathbf{R}'}(E) H_{\mathbf{R}', \mathbf{R}_l} \\ &= \sum_{\mathbf{R}'} [\phi_{\mathbf{R}_0}(\mathbf{r}_{\mathbf{R}_0}) + \phi_{\mathbf{R}_0}(\mathbf{r}_{\mathbf{R}_0})(E - E_{\nu, \mathbf{R}_0})] \\ & \quad \times G_{\mathbf{R}_0, \mathbf{R}'}(E) H_{\mathbf{R}', \mathbf{R}_l}. \end{aligned} \quad (\text{A3})$$

Applying this formula to Eq. (6) we obtain expression (16). If the width of the central region is large enough, so that all charge and potential relaxations take place in the central region, the value of the lesser Green's function defined by Eq. (7) does not depend on the choice of how we partitioned our system into leads and the central region. Thus, we may use formula (16) for the charge density even if we calculate the site-diagonal elements of the lesser Green's function for a smaller central region, without the assumption of vanishing coefficients $h_{\mathbf{R}_0, \mathbf{R}_l}$.

APPENDIX B

In this Appendix we will rewrite expression (42) for the transmission coefficient in terms of auxiliary Green's functions. To address this problem let us consider the following function of energy:

$$\begin{aligned} \tilde{T}(E) &= \frac{1}{2} \text{Tr}[[Q^0, H][G(E_+) - G(E_-)] \\ & \quad \times [Q^N, H][G(E_+) - G(E_-)]], \end{aligned} \quad (\text{B1})$$

where we use full matrix notation. $\text{Tr}\{\dots\}$ in Eq. (B1) means trace over indices \mathbf{BL} and over index of principal layer p which runs from $-\infty$ to ∞ . We will show that the right-hand side of Eqs. (42) and (B1) coincide with each other. Opening the commutators in Eq. (B1) the expression for $\tilde{T}(E)$ can be rewritten as

$$\begin{aligned} \tilde{T}(E) &= \frac{1}{2} \sum_{\mu, \nu} \sum_{l < 1} \sum_{c=1}^N \sum_{c'=1}^N \sum_{r > N} (-1)^{\mu+\nu} \text{tr}\{H_{c,l} G_{l,r}(z_\mu) \\ & \quad \times H_{r,c'} G_{c',c}(z_\nu) + H_{l,c} G_{c,c'}(z_\mu) H_{c',r} G_{r,l}(z_\nu) \\ & \quad - H_{c,l} G_{l,c'}(z_\mu) H_{c',r} G_{r,c}(z_\nu) \\ & \quad - H_{l,c} G_{c,r}(z_\mu) H_{r,c'} G_{c',l}(z_\nu)\}. \end{aligned} \quad (\text{B2})$$

Here indices μ, ν run from 1 to 2 and complex energies are defined as $z_1 = E_+$, and $z_2 = E_-$.

Using the Dyson equations

$$\begin{aligned} G_{r,c}(z) &= \sum_{r' > N} \sum_{s'=1}^N G_{r,r'}^{\mathcal{R}}(z) H_{r',c'} G_{c',c}(z), \\ G_{c,r}(z) &= \sum_{r' > N} \sum_{s'=1}^N G_{c,c'}(z) H_{c',r'} G_{r',r}^{\mathcal{R}}(z), \\ G_{r,l}(z) &= \sum_{r' > N} \sum_{c'=1}^N G_{r,r'}^{\mathcal{R}}(z) H_{r',c'} G_{c',l}(z), \\ G_{l,r}(z) &= \sum_{l' < 1} \sum_{c'=1}^N G_{l,l'}^{\mathcal{L}}(z) H_{l',c'} G_{c',r}(z), \end{aligned} \quad (\text{B3})$$

Dyson Eqs. (22) for $G_{l,s}(z)$ and $G_{s,l}(z)$, the definitions (11) and (12) of self-energies $\Sigma_{c,c'}^{\mathcal{L}}$ and $\Sigma_{c,c'}^{\mathcal{R}}$, and cyclic invariance of the trace, Eq. (B2) can be recast as

$$\begin{aligned} \tilde{T}(E) &= \frac{1}{2} \sum_{\mu, \nu} \sum_{c_1=1}^N \sum_{c_2=1}^N \sum_{c_3=1}^N \sum_{c_4=1}^N (-1)^{\mu+\nu} \\ & \quad \times \text{tr}\{[\Sigma_{c_1, c_2}^{\mathcal{L}}(z_\mu) - \Sigma_{c_1, c_2}^{\mathcal{L}}(z_\nu)] G_{c_2, c_3}(z_\mu) \\ & \quad \times [\Sigma_{c_3, c_4}^{\mathcal{R}}(z_\mu) - \Sigma_{c_3, c_4}^{\mathcal{R}}(z_\nu)] G_{c_4, c_1}(z_\nu)\}. \end{aligned} \quad (\text{B4})$$

Only two terms, one with $\mu=1, \nu=2$, and another with $\mu=2, \nu=1$, do not vanish in Eq. (B4). These two terms are actually equal to one another. The last statement follows from the fact that the trace of four matrices can be expressed in terms of transposed matrices as

$$\text{tr}\{ABCD\} = \text{tr}\{D^T C^T B^T A^T\} = \text{tr}\{A^T D^T C^T B^T\},$$

and that Hamiltonian (4) is a symmetric matrix $H^T = H$, so all matrices $G, G^{\mathcal{L}}, G^{\mathcal{R}}, \Sigma^{\mathcal{L}}$, and $\Sigma^{\mathcal{R}}$ are also symmetric. Applying the definition of the $\Gamma^{\mathcal{L}/\mathcal{R}}$ matrices (10) to expression (B4) one can see that the right hand sides of Eqs. (B4) and (42) in fact coincide, proving the equality $\tilde{T}(E) = T(E, V)$.

Equation (B1) can be rewritten by using the expression (26) for the commutator

$$\begin{aligned} \tilde{T}(E) &= \frac{1}{2} \text{Tr}\{[Q^0, S^\alpha][M(E_+) - M(E_-)] \\ & \quad \times [Q^N, S^\alpha][M(E_+) - M(E_-)]\}, \end{aligned} \quad (\text{B5})$$

where

$$M(z) = [1 + (\alpha - \gamma) S^\alpha]^{-1} \sqrt{\Delta}(z - H)^{-1} \sqrt{\Delta}[1 + S^\alpha(\alpha - \gamma)]^{-1}. \quad (\text{B6})$$

Using the explicit form (25) of the Hamiltonian, the matrix $M(z)$ can be transformed as

$$\begin{aligned}
 M(z) &= [1 + (\alpha - \gamma)S^\alpha]^{-1} \{ (z - C)\Delta^{-1} \\
 &\quad + S^\alpha [(\alpha - \gamma)(z - C)\Delta^{-1} - 1] \}^{-1} \\
 &= \{ (z - C)[\Delta + (\gamma - \alpha)(z - C)]^{-1} - S^\alpha \}^{-1} \\
 &\quad + [1 + (\alpha - \gamma)S^\alpha]^{-1} (\alpha - \gamma) \\
 &= g^\alpha(z) + [1 + (\alpha - \gamma)S^\alpha]^{-1} (\alpha - \gamma). \tag{B7}
 \end{aligned}$$

The last term in the last line in Eq. (B7) is z independent and cancels in Eq. (B5). Thus, Eq. (B5) takes the form

$$\begin{aligned}
 \tilde{T}(E) &= \frac{1}{2} \text{Tr} \{ [Q^0, S^\alpha] [g^\alpha(E_+) - g^\alpha(E_-)] \\
 &\quad \times [Q^N, S^\alpha] [g^\alpha(E_+) - g^\alpha(E_-)] \}. \tag{B8}
 \end{aligned}$$

Algebraically, this expression looks exactly the same as Eq. (B1) with $P^\alpha(z) - S^\alpha$ taking the place of $z - H$. Similarly, the equivalent to Eq. (42) is Eq. (43), where we used the equality $\tilde{T}(E) = T(E, V)$.

*Electronic address: sfaleev@sandia.gov

†Present address: Cornell Nanoscale Science and Technology Facility, Ithaca, NY 14853.

¹N. D. Lang, Phys. Rev. B **52**, 5335 (1995).

²K. Hirose and M. Tsukada, Phys. Rev. B **51**, 5278 (1995).

³Y. Xue, S. Datta, and M. A. Ratner, J. Chem. Phys. **115**, 4292 (2001).

⁴S. N. Yaliraki, A. E. Roitberg, C. Gonzalez, V. Mujica, and M. A. Ratner, J. Chem. Phys. **111**, 6997 (1999).

⁵P. A. Derosa and J. M. Seminario, J. Phys. Chem. B **105**, 471 (2001).

⁶J. J. Palacios, A. J. Perez-Jimenez, E. Louis, and J. A. Verges, Phys. Rev. B **64**, 115411 (2001).

⁷J. Heurich, J. C. Cuevas, W. Wenzel, and G. Schon, Phys. Rev. Lett. **88**, 256803 (2002).

⁸Y. Xue, S. Datta, and M. A. Ratner, Chem. Phys. **281**, 151 (2002).

⁹Y. Xue and M. A. Ratner, Phys. Rev. B **68**, 115406 (2003).

¹⁰J. M. Seminario, L. E. Cordova, and P. A. Derosa, Proc. IEEE **91**, 1958 (2003).

¹¹F. Evers, F. Weigend, and M. Koentopp, Phys. Rev. B **69**, 235411 (2004).

¹²X. Zhang, L. Fonseca, and A. A. Demkov, Phys. Status Solidi B **233**, 70 (2002).

¹³J. Tomfohr and O. F. Sankey, J. Chem. Phys. **120**, 1542 (2004).

¹⁴J. Li, J. K. Tomfohr, and O. F. Sankey, Photonics Spectra **19**, 133 (2003).

¹⁵J. Li, J. K. Tomfohr, and O. F. Sankey, Phys. Status Solidi B, **239**, 80 (2003).

¹⁶P. S. Damle, A. W. Ghosh, and S. Datta, Phys. Rev. B **64**, 201403(R) (2001).

¹⁷J. Taylor, H. Guo, and J. Wang, Phys. Rev. B **63**, 121104(R) (2001).

¹⁸J. Taylor, H. Guo, and J. Wang, Phys. Rev. B **63**, 245407 (2001).

¹⁹M. Brandbyge, J.-L. Mozos, P. Ordejon, J. Taylor, and K. Stokbro, Phys. Rev. B **65**, 165401 (2002).

²⁰P. S. Damle, A. Ghosh, and S. Datta, Chem. Phys. **281**, 171 (2002).

²¹H. Mehrez, A. Wlasenko, B. Larade, J. Taylor, P. Grutter, and H. Guo, Phys. Rev. B **65**, 195419 (2002).

²²K. Stokbro, J. Taylor, M. Brandbyge, and P. Orejon, Ann. N.Y. Acad. Sci. **1006**, 212 (2003).

²³J.-L. Mozos, P. Ordejon, M. Brandbyge, J. Taylor, and K. Stokbro, Nanotechnology **13**, 346 (2002).

²⁴J. Taylor, M. Brandbyge, and K. Stokbro, Phys. Rev. Lett. **89**,

138301 (2002).

²⁵S. K. Nielsen, M. Brandbyge, K. Hansen, K. Stokbro, J. M. van Ruitenbeek, and F. Besenbacher, Phys. Rev. Lett. **89**, 066804 (2002).

²⁶K. Stokbro, J. Taylor, M. Brandbyge, J.-L. Mozos, and P. Ordejon, Comput. Mater. Sci. **27**, 151 (2003).

²⁷M. Brandbyge, K. Stokbro, J. Taylor, J.-L. Mozos, and P. Ordejon, Phys. Rev. B **67**, 193104 (2003).

²⁸K. Stokbro, J. Taylor, and M. Brandbyge, J. Am. Chem. Soc. **125**, 3674 (2003).

²⁹J. Taylor, M. Brandbyge, and K. Stokbro, Phys. Rev. B **68**, 121101(R) (2003).

³⁰O. K. Andersen and O. Jepsen, Phys. Rev. Lett. **53**, 2571 (1984).

³¹J. Kudrnovsky, V. Drchal, C. Blaas, P. Weinberger, I. Turek, and P. Bruno, Phys. Rev. B **62**, 15 084 (2000).

³²I. Turek, J. Kudrnovsky, V. Drchal, L. Szunyogh, and P. Weinberger, Phys. Rev. B **65**, 125101 (2002).

³³G. Kresse, W. Bergermayer, and R. Podloucky, Phys. Rev. B **66**, 146401 (2002).

³⁴J. Kudrnovsky, V. Drchal, I. Turek, C. Blaas, P. Weinberger, and P. Bruno, Surf. Sci. **454**, 918 (2000).

³⁵D. A. Stewart and M. van Schilfgaarde, J. Appl. Phys. **93**, 7355 (2003).

³⁶K. D. Belashchenko, E. Y. Tsymbal, M. van Schilfgaarde, D. A. Stewart, I. I. Oleinik, and S. S. Jaswal, Phys. Rev. B **69**, 174408 (2004).

³⁷M. van Schilfgaarde and W. R. L. Lambrecht, in *Tight-Binding Approach to Computational Materials Science*, edited by L. Colombo, A. Gonis, and P. Turchi, MRS Symposia Proceedings No. 491 (Materials Research Society, Pittsburgh, 1998).

³⁸M. Methfessel, M. van Schilfgaarde, and R. A. Casali, *Electronic Structure and Physical Properties of Solids: The Uses of the LMTO Method*, Lecture Notes in Physics Vol. 535 (Springer-Verlag, Berlin, 2000).

³⁹O. K. Andersen, Phys. Rev. B **12**, 3060 (1975).

⁴⁰I. Turek, V. Drchal, J. Kudrnovsky, M. Sob, and P. Weinberger, *Electronic Structure of Disordered Alloys, Surfaces and Interfaces* (Kluwer, Dordrecht, 1997).

⁴¹G. D. Mahan, *Many-Particle Physics* (Plenum, New York, 1981).

⁴²R. Lake, G. Klimeck, R. C. Bowen, and D. Jovanovic, J. Appl. Phys. **81**, 7845 (1997).

⁴³H. L. Skriver and N. M. Rosengaard, Phys. Rev. B **43**, 9538 (1991).

⁴⁴B. Wenzien, J. Kudrnovsky, V. Drchal, and M. Sob, J. Phys.: Condens. Matter **1**, 9893 (1989).

- ⁴⁵M. P. Lopez Sancho, J. M. Lopez Sancho, and J. Rubio, *J. Phys. F: Met. Phys.* **15**, 851 (1985).
- ⁴⁶Y. Meir and N. S. Wingreen, *Phys. Rev. Lett.* **68**, 2512 (1992).
- ⁴⁷M. A. Reed, C. Zhou, C. J. Muller, T. P. Burgin, and J. M. Tour, *Science* **278**, 252 (1997).
- ⁴⁸M. Dorogi, J. Gomez, R. Osifchin, R. P. Andres, and R. Reifenberger, *Phys. Rev. B* **52**, 9071 (1995).
- ⁴⁹X. Xiao, B. Xu, and N. J. Tao, *Nano Lett.* **4**, 267 (2004).
- ⁵⁰E. G. Emberly and G. Kirczenow, *Phys. Rev. B* **64**, 235412 (2001).
- ⁵¹M. Di Ventra, S. T. Pantelides, and N. D. Lang, *Phys. Rev. Lett.* **84**, 979 (2000).
- ⁵²E. G. Emberly and G. Kirczenow, *Phys. Rev. B* **58**, 10 911 (1998).
- ⁵³A. M. Bratkovsky and P. E. Kornilovitch, *Phys. Rev. B* **67**, 115307 (2003).
- ⁵⁴J. Nara, W. T. Geng, H. Kino, N. Kobayashi, and T. Ohno, *J. Chem. Phys.* **121**, 6485 (2004).
- ⁵⁵G. Kresse and J. Furthmuller, *Phys. Rev. B* **54**, 11 169 (1996).
- ⁵⁶M. Di Ventra, S. T. Pantelides, and N. D. Lang, *Phys. Rev. Lett.* **88**, 046801 (2002).
- ⁵⁷Y.-C. Chen, M. Zwolak, and M. Di Ventra, *Nano Lett.* **4**, 1709 (2004).
- ⁵⁸S. V. Faleev, M. van Schilfgaarde, and T. Kotani, *Phys. Rev. Lett.* **93**, 126406 (2004).
- ⁵⁹O. Jepsen and O. K. Andersen, *Z. Phys. B: Condens. Matter* **97**, 35 (1995).
- ⁶⁰J. M. van Ruitenbeek, *Metal Clusters on Surfaces: Structure, Quantum Properties, Physical Chemistry, Cluster Physics* (Springer-Verlag, Heidelberg, 2000), pp. 175–210.
- ⁶¹B. Ludoph and J. M. van Ruitenbeek, *Phys. Rev. B* **61**, 2273 (2000).
- ⁶²M. Brandbyge, J. Schiøtz, M. R. Sørensen, P. Stoltze, K. W. Jacobsen, J. K. Nørskov, L. Olesen, E. Laegsgaard, I. Stensgaard, and F. Besenbacher, *Phys. Rev. B* **52**, 8499 (1995).
- ⁶³C. Sirvent, J. G. Rodrigo, S. Vieira, L. Jurczyszyn, N. Mingo, and F. Flores, *Phys. Rev. B* **53**, 16 086 (1996).
- ⁶⁴H. Yasuda and A. Sakai, *Phys. Rev. B* **56**, 1069 (1997).
- ⁶⁵R. H. M. Smit, C. Untiedt, A. I. Yanson, and J. M. van Ruitenbeek, *Phys. Rev. Lett.* **87**, 266102 (2001).